1 **Wall teichoic acids regulate peptidoglycan synthesis by paving cell wall nanostructure**

2 Felix Barber[1], Zarina Akbary[1], Zhe Yuan[1], Jacob Biboy[2], Waldemar Vollmer[3], Enrique R. Rojas[1,*]

3 1: Center for Genomics and Systems Biology, New York University, New York 10003, United States.

4 2: Center for Bacterial Cell Biology, Newcastle University, Newcastle upon Tyne NE2 4AX, United

5 Kingdom.

6 3: Institute for Molecular Bioscience, The University of Queensland, Brisbane, Australia.

7

8 *Correspondence: rojas@nyu.edu

9

10 **Keywords:** Rod complex, bacterial growth, cell shape, morphogenesis, *Bacillus subtilis*

Summary

The cell wall is a polymeric exoskeleton that defines the size and shape of bacteria; it is composed of peptidoglycan and, in Gram-positive bacteria, wall teichoic acid polymers. Two systems synthesize peptidoglycan in rod-shaped bacteria, which are found pervasively across bacterial clades: the multi-protein Rod complexes synthesize anisotropic peptidoglycan, which is required for rod shape because it reinforces the cell wall along its circumference[1–3], whereas the non-essential enzyme PBP1 synthesizes isotropic peptidoglycan[1,4] (Fig. 1A). In Gram-positive bacteria, rod shape also requires wall teichoic acids[5] for unknown reasons. Here, we show that wall teichoic acids promote rod shape by preventing the formation of nanoscopic pores in the *Bacillus subtilis* cell wall, which lead to amorphous growth by activating PBP1 and inhibiting Rod complexes. Depleting wall teichoic acids resulted in pores within minutes, coinciding with a rapid increase in PBP1-mediated synthesis. PBP1's ability to sustain teichoic acid-less growth depended on its intrinsically disordered domain. In contrast to previous steady-state measurements[6,7], we found that wall teichoic acid depletion caused the transient arrest of Rod complexes prior to the onset of amorphous growth. Finally, one of the two synthetically lethal cell wall hydrolases in *B. subtilis*[8], LytE, became essential during wall teichoic acid depletion, meaning that PBP1 and LytE execute a novel, amorphous mode of growth. Collectively, our results identify the cell wall, via its molecular-scale structure, as a non-canonical auto-regulator of its own synthesis.

33 **Introduction**

34 The bacterial cell wall is a solid polymeric macromolecule that protects cells from lysis in many contexts,
35 including osmotic shock[9], pathogenesis[10] and antibiotic treatment[11]. The cell wall also prescribes cell
36 shape (Fig. 1A), which affects many aspects of cellular physiology[3,12,13] — a pervasive shape across bacteria
37 is the bacillus, or "rod"[14]. The cell wall consists primarily of peptidoglycan: glycan polymers that are
38 covalently crosslinked through short peptides. In Gram-positive bacteria, peptidoglycan is also covalently
39 modified with wall teichoic acids, anionic polymers of sugar alcohol-phosphate subunits (hereafter
40 "teichoic acids," distinct from the membrane-anchored lipoteichoic acids)[15,16]. Teichoic acids are usually
41 nonessential[5,17], however, inhibiting their synthesis causes *Bacillus subtilis* and *Listeria monocytogenes* to
42 grow slowly[5] and amorphously[17,18]. How teichoic acids enable rod-shaped morphogenesis is
43 unknown[5,17,18].

44

45 During rod-shaped cell growth, peptidoglycan is synthesized by two molecular mechanisms. First, the
46 essential, multi-protein Rod complexes synthesize anisotropic peptidoglycan that structurally reinforces
47 the cell wall along its circumference (Fig. 1A), providing the mechanical basis for rod shape[1,2]. Anisotropic
48 peptidoglycan synthesis results from the processive circumferential motion of Rod complexes along the
49 plasma membrane[19–21]. In *B. subtilis*, this motion is oriented by actin homologs MreB, Mbl and
50 MreBH[22,23,6], and is driven by peptidoglycan synthesis itself[19]. Circumferential motion, therefore, is a direct
51 indicator for Rod complex activity[24,25]. Within the Rod complex, peptidoglycan polymerization is catalyzed
52 by the transglycosylase RodA[26], drawing from lipid II precursors in the plasma membrane, while cross-
53 linking of nascent polymers to acceptor peptides within the existing cell wall is catalyzed by the
54 transpeptidases PBP2A and PBPH[4,27] ("Class B" PBPs).

55

56 The second mechanism is the non-essential, multi-domain enzyme PBP1 (a "Class A" PBP, encoded by
57 *ponA*[28]) that synthesizes isotropic peptidoglycan (Fig. 1A). PBP1 is thought to repair pores in the cell wall
58 that arise during the rapid cell-wall turnover required for cell growth[4,29]. Because Rod complexes
59 synthesize peptidoglycan anisotropically and PBP1 synthesizes it isotropically, the balance of their
60 expression determines cell width[1], and overexpression of PBP1 causes semi-amorphous growth[1].

61

62 Teichoic acids influence diverse cellular phenotypes including antimicrobial resistance[30,31], protein
63 localization within the cell envelope[32], pathogenesis[33], cation homeostasis[34,35] and autolysis[36–39]. It is
64 unclear, however, how these processes would account for the dependence of cell shape on teichoic acids
65 according to the Rod complex-PBP1 model. One possibility is that Rod complexes are directly,
66 biochemically activated by teichoic acids[40]. This model is consistent with the observations that teichoic
67 acid synthases and peptidoglycan synthesis machinery both exhibit punctate spatial patterning[41], and that
68 the syntheses of the two materials are co-local in both *B. subtilis*[42] and *Streptococcus pneumoniae*[43].
69 However, teichoic acid synthases do not exhibit the circumferential motion characteristic of Rod
70 complexes, and Rod complexes move processively along the cell membrane in amorphous cells depleted
71 for TagO, the enzyme that catalyzes the first committed reaction of teichoic acid synthesis[6,7]. Given these
72 conflicting data, there is no known mechanistic interaction between teichoic acids and either of the two
73 peptidoglycan biosynthesis pathways.

74

75

76 **Results**

77 **Inhibiting wall teichoic acid synthesis reduces growth rate prior to cell shape loss**

78 *Bacillus subtilis* mutants that lack teichoic acids (Δ*tagO*) grow amorphously and ≈4 times slower than
79 wild-type cells in bulk liquid culture[5]. To interrogate this dependence at the single-cell level, we measured
80 the dynamics of growth rate and cell shape upon teichoic acid depletion by using microfluidics to acutely
81 treat exponentially growing, wild-type *B. subtilis* cells with the small molecule tunicamycin (Fig. 1B), which
82 specifically inhibits TagO at low concentrations[31,44–46] (Fig. S1A,B,C). Approximately 10 minutes after
83 tunicamycin treatment, the median growth rate decreased from its steady-state value in rich medium
84 (LB), plateaued temporarily, and then decreased a second time until it reached its steady-state value in
85 tunicamycin (Fig. 1B, S2A). Cells retained their untreated rod shape until the second decrease in
86 elongation rate when they began to widen, eventually losing rod shape altogether (Fig. S2B). Amorphous
87 cells grew indefinitely (Video S1). We observed a similar decline in the single-cell growth rate prior to the
88 loss of cell shape when we acutely inhibited *tagO* transcription (Fig. S2C,D), during tunicamycin treatment
89 on agarose pads (Fig. S2E,F), and during tunicamycin treatment in minimal media (S750; Fig. S2G,H;
90 *Methods*).

91

92 **Inhibiting wall teichoic acid synthesis reduces Rod complex activity**

93 Although it was previously reported that inhibiting teichoic acid synthesis does not prevent Rod complex
94 motion during steady-state, amorphous cell growth[6,7], we hypothesized that the loss of cell shape results
95 from a quantitative or transient effect of teichoic acid depletion on Rod complex activity. To test this, we
96 measured the dynamics of Rod complex motion upon tunicamycin treatment by using total internal
97 reflection fluorescence microscopy to track a fusion of superfolder GFP and MbI[19,24,25], a protein scaffold
98 of the Rod complex. As we hypothesized, tunicamycin caused an acute decrease in the percentage of Rod

99 complexes that moved processively, (Fig. 1C), in the spatial density of processive Rod complexes (Fig. S3A),
100 and in Rod complex speed (Fig. S3B). These decreases were coincident with the first decline in cellular
101 growth rate (Fig. 1B). Following the second decrease in growth rate (and loss of cell shape; Fig. 1B) we
102 observed a small but reproducible recovery of Rod complex motion (Fig. 1C) against a higher background
103 of diffuse Mbl-sfGFP fluorescence than we observed in untreated cells (Fig. S3C, Videos S2-S7), consistent
104 with the previous observation of Rod complex motion in Δ*tagO* mutants[6]. Tunicamycin also inhibited Rod
105 complex motion as tracked via another Rod complex scaffold (MreB-mNeonGreen; Fig. S3D-F), and
106 inhibited Rod complexes in slow-growing cells in minimal media (S3G-I; *Methods*). Finally, like tunicamycin
107 treatment, transcriptional inhibition of *tagO* expression caused a decrease in each metric for Rod complex
108 activity (Fig. S3J-L). The decrease was more gradual for transcriptional inhibition, which we expected since
109 in this case TagO enzymes must be diluted by growth before teichoic acids are depleted.

110

111 Since Rod complexes synthesize peptidoglycan uniformly across the cell length, we hypothesized that this
112 distributed synthesis would be perturbed upon the Rod complex arrest associated with teichoic acid
113 depletion. To test this, we measured the localization of peptidoglycan synthase activity. First, we pulsed
114 exponentially growing cells with the fluorescent D-amino acid 7-hydroxycoumarin-3-carboxylic acid-
115 amino-D-alanine (HADA), which is incorporated into peptidoglycan by transpeptidases[47,48], for 5 min at
116 various times after tunicamycin treatment. Whereas in untreated cells HADA was incorporated uniformly
117 across the cell wall, tunicamycin treatment caused HADA to be incorporated as aberrant puncta (Fig. 1D),
118 consistent with a loss of distributed Rod complex synthesis. Tunicamycin had the same effect on the
119 dipeptide D-amino acid ethynyl-D-alanine D-alanine (EDA-DA), which is incorporated into peptidoglycan
120 precursors cytosolically[49] (Fig. S4B). Finally, transcriptional inhibition of *tagO* also caused punctal HADA
121 incorporation (Fig. S4A).

122

123 Since Rod complexes are the primary mode of peptidoglycan synthesis during vegetative growth, we
124 hypothesized that a loss of Rod complex activity during teichoic acid depletion would require increased
125 peptidoglycan synthesis by another mechanism, and that this shift would cause changes in the abundance
126 of specific types of peptidoglycan crosslinks. To test this, we performed high performance liquid
127 chromatography on purified, lysozyme-digested peptidoglycan from exponentially growing wild-type and
128 Δ*tagO* cells[50]. Deleting *tagO* caused a small increase in the percentage of un-cross-linked peptidoglycan
129 subunits, and a corresponding decrease in the percentage of dimeric cross-links (Fig. 1E, S5A). Conversely,
130 we observed increases in trimeric and tetrameric cross-links in Δ*tagO* cells that were reproducible but not
131 significant across two replicates (Trimers: 9.9% ± 0.1% for Δ*tagO* vs. 8.0% ± 0.7% for wild-type. Tetramers:
132 1.6% ± 0.2% for Δ*tagO* vs. 0.8% ± 0.1% for wild-type. Error is s.e.m.; Fig. S5B,C,D). The correlation of
133 trimeric and tetrameric cross-linking with reduced Rod complex activity is consistent with a previous study
134 that reported the reduction of these species in Δ*ponA* cells[50].

135

136 **PBP1 is essential in the absence of wall teichoic acids**

137 Since i) Rod complexes and PBP1 are the two principal modes of peptidoglycan synthesis during cell
138 growth, ii) teichoic acid depletion acutely inhibits Rod complex activity (Fig. 1C), and iii) cells lacking
139 teichoic acids grow amorphously with a cell wall that is rich in trimeric and tetrameric cross-links, as would
140 be expected from PBP1-mediated cell growth, we hypothesized that teichoic acid-less growth is driven by
141 PBP1. To test this, we first measured the effect of tunicamycin treatment on the growth, shape, and
142 viability of Δ*ponA* mutants. At the single-cell level, tunicamycin caused a decrease in the growth rate of
143 Δ*ponA* cells equivalent to the growth-rate decrease it caused in wild-type cells, except without the
144 transient plateau and subsequent shape loss (Fig. 2A). Rather, Δ*ponA* mutants exhibited pervasive lysis

145 after their growth rate decrease (Fig. 2B). Furthermore, concentrations of tunicamycin that permitted
146 amorphous growth of wild-type cells prevented growth of Δ*ponA* cells (Fig. 2C, S6A).

147

148 Teichoic acid-less cell growth was dependent on the glycosyltransferase activity of PBP1, since a mutant
149 incapable of this reaction (*ponA*$_{GT-}$) did not grow at concentrations of tunicamycin that permitted wild-
150 type growth (Fig. 2C; *Methods*). Similarly, tunicamycin inhibited the growth of a PBP1 mutant incapable
151 of transpeptidation (*ponA*$_{TP-}$; Fig. S6B)[51] 40-times more strongly than wild-type growth (Fig. 2C), and
152 caused only partial shape loss of this mutant prior to growth arrest (Fig. 2A inset). Tunicamycin may inhibit
153 the growth of the *ponA*$_{GT-}$ mutant more than it inhibits that of the *ponA*$_{TP-}$ mutant because PBP1
154 transpeptidase activity is dependent on glycosyltransferase activity[52]. In addition to its catalytic domains,
155 PBP1 also possesses a highly anionic 14kDa C-terminal intrinsically disordered domain, which stimulates
156 PBP1-mediated synthesis upon cell wall damage[29]; we found that tunicamycin inhibited the growth of a
157 mutant harboring a version of PBP1 lacking this domain (*ponA*$_{\Delta IDR}$; Fig. 2C, S6B). Finally, transcriptional
158 inhibition of *tagO* expression in Δ*ponA* and *ponA*$_{TP-}$ mutant backgrounds prevented growth in bulk culture
159 (Fig. S6C).

160

161 These results demonstrate that PBP1 activity is essential for the amorphous cell growth following teichoic
162 acid depletion, which inhibits Rod complexes. In this light, we hypothesized that amorphous growth would
163 require increased peptidoglycan synthesis by PBP1 upon teichoic acid depletion, concomitant with the
164 decline in Rod complex activity (Fig. 1C). To test this, we performed single-molecule tracking on a PBP1-
165 mNeonGreen fusion protein expressed at low levels, in addition to the native enzyme (Fig. 2D, S6D;
166 *Methods*). Previous studies demonstrated that PBP1 is stationary when it is actively synthesizing
167 peptidoglycan and rapidly diffuses when it is not[4]. Consistent with our hypothesis, we observed a stark

168 decline in PBP1 diffusion upon tunicamycin treatment, culminating in large, stable PBP1 puncta (Fig. 2D,
169 Videos S8-9).

170

171 To confirm that these PBP1 puncta were enzymatically active, we performed HADA staining after 90
172 minutes of tunicamycin treatment and measured the colocalization of PBP1 and HADA puncta. We found
173 that 67% of PBP1 puncta overlapped with HADA puncta, while a simulated random localization yielded an
174 overlap of only 36% (Fig. S6E). Furthermore, Δ*ponA* cells treated with tunicamycin did not display HADA
175 puncta (Fig. 1D), indicating that these puncta resulted from PBP1-polymerized peptidoglycan. However,
176 $ponA_{TP-}$ cells exhibited only a partial reduction in HADA puncta labelling compared to wild-type (Fig. 1D),
177 suggesting that other transpeptidases may partially complement PBP1 transpeptidation during teichoic
178 acid depletion. This is consistent with the incomplete growth inhibition of tunicamycin-treated $ponA_{TP-}$
179 cells, as opposed to the full arrest of tunicamycin-treated Δ*ponA* and $ponA_{GT-}$ cells (Fig. 2C).

180

181 To test whether PBP1 expression increases in concert with PBP1-mediated synthesis upon teichoic acid
182 depletion, we measured PBP1 abundance by western blot (Fig. 2E), and by labeling with the fluorescent
183 penicillin bocillin, which covalently binds transpeptidases at their active sites[53] (Fig. S6F-H). Upon
184 tunicamycin treatment, we observed a similar increase in PBP1 levels as measured with each assay (62%
185 ± 8% by western blot, 80% ± 6% by bocillin labeling. Errors are s.e.m.). Notably, the increase in PBP1
186 bocillin labeling preceded the increase in PBP1 staining by western blot (Fig. S6H), on the same timescale
187 as decreased PBP1 diffusion/synthesis. The increase in PBP1 expression did not result from the SigI stress
188 response that is triggered by teichoic acid depletion[54], since we also observed increased PBP1 expression
189 in Δ*sigI* mutant cells (Fig. S6I).

190

191

192 Our results demonstrate that teichoic acid depletion causes an increase in PBP1 abundance and PBP1-
193 mediated synthesis, and that this enzyme becomes essential for growth without teichoic acids. Based on
194 previous studies[1], the increase in PBP1 expression that we measured is, alone, insufficient to cause the
195 degree of cell shape changes that we observed. Since our single-molecule measurements indicate that
196 PBP1-mediated synthesis increases upon teichoic acid depletion, our data are consistent with a model in
197 which teichoic acids inhibit peptidoglycan synthesis by PBP1 such that when teichoic acids are depleted
198 PBP1 outcompetes Rod complex for lipid II precursors leading to slow, amorphous cell growth and Rod
199 complex inhibition.

200

201 Given this model, we next questioned whether Rod complex motion also decreases in the absence of
202 PBP1. We assayed Rod complex motion during tunicamycin treatment in Δ*ponA* cells (*Methods*), finding
203 that Rod complex motion declined, but with a delay compared to wild-type cells (Fig. 2F, Videos S10-S11).
204 In this case, a mechanism besides competition for precursors must inhibit Rod complex function during
205 teichoic acid depletion.

206

207 **Teichoic acid depletion results in a porous cell wall in the absence of PBP1**

208 We next asked why PBP1 becomes activated during teichoic acid depletion, and why Rod complexes arrest
209 during teichoic acid depletion in Δ*ponA* cells. Since PBP1 is thought to fill pores in the cell wall[4] and is
210 conditionally essential in the absence of teichoic acids, we hypothesized that teichoic acids play a
211 complementary pore-filling role and that Rod complexes require a pore-less "confluent" cell wall on which
212 to synthesize new peptidoglycan. Furthermore, since intrinsically disordered domains sense cell wall

213 damage[29], likely through entropic translocation through pores in the cell wall[55], and deleting PBP1's
214 intrinsically disordered region prevents growth during teichoic acid depletion (Fig. 2C), we additionally
215 hypothesized that PBP1-mediated synthesis is stimulated by this domain when it senses natural pores in
216 the teichoic acid-less cell wall.

217

218 To test whether depleting teichoic acids results in pores within the cell wall, we leveraged a single-cell
219 microfluidics assay we recently developed[56]. In this assay, we used a brief pulse of detergent to lyse cells
220 expressing genetically encoded, cytosolic fluorescent probes and then measured the kinetics of the
221 probes' diffusion through the cell wall at the single-cell level — this provides an empirical measurement
222 of cell wall permeability (*Methods*). To measure the pore structure at different length scales, we used two
223 probes: mNeonGreen (27.5 kDa, minimal radius R_{min}≈2.0 nm[57]) and a new fluorogenic version of ubiquitin
224 that we developed (ubiquitin-FlAsH, 9.5 kDa, R_{min}≈1.4 nm).

225

226 We first measured the effect of teichoic acid depletion on cell wall permeability by treating wild-type and
227 Δ*ponA* cells with tunicamycin (Fig. 3A). To avoid confounding effects on cell wall permeability caused by
228 changes in peptidoglycan synthesis, we measured permeability before Rod complex activity began to
229 decline (10 min for WT and 20 min for Δ*ponA*). Contrary to our initial hypothesis, tunicamycin treatment
230 of wild-type cells resulted in a modest but reproducible decrease in the permeability of wild-type cell
231 walls, as measured with the mNeonGreen probe (Fig. 3A, S7A). Conversely, the same treatment resulted
232 in an increase in permeability in Δ*ponA* cells.

233

234 As an alternative approach to remove teichoic acids, we perfused cells with a purified phosphodiesterase,
235 GlpQ, that *B. subtilis* naturally expresses during phosphate starvation to digest and recycle its teichoic
236 acids[58] (*Methods*). Perfusing cells with GlpQ dissolved in phosphate buffer saline (PBS) for 15 minutes
237 reduced the abundance of teichoic acids within the cell wall (Fig. S8; *Methods*) and recapitulated the effect
238 of tunicamycin on cell wall permeability: it caused a modest decrease in mNeonGreen permeability in
239 wild-type cells but a large increase in permeability in Δ*ponA* cells (Fig. 3B, S7B). Together, these results
240 are consistent with a model in which teichoic acids occlude pores in the cell wall, and in which PBP1 is
241 activated by these pores via its intrinsically disordered domain to "seal" them, thereby preventing an
242 increase in cell wall permeability[56].

243

244 Treating Δ*ponA* cells with tunicamycin or GlpQ for durations approaching the cell-cycle time (≈20 min)
245 could cause pore formation indirectly, for example, by inducing peptidoglycan hydrolysis unbalanced by
246 synthesis[36–39]. To control for this possibility, we measured cell-wall permeability during teichoic acid
247 digestion by GlpQ, reasoning that at short time scales after teichoic acid digestion, peptidoglycan
248 hydrolases would not have had time to meaningfully enlarge pores. Because we anticipated small,
249 incipient pores, we used our ubiquitin probe to test for them. When we simultaneously digested teichoic
250 acids and measured the loss of this probe in Δ*ponA* cells, we observed an increase in cell wall permeability
251 within 2 minutes of GlpQ treatment (Fig. 3C, S7C, S9A,B).

252

253 In concurrent work, we discovered that the size threshold for cell wall permeability is close to the size of
254 typical globular proteins[56]. We therefore hypothesized that the pores exposed during teichoic acid
255 depletion would cause increased labeling by peptidoglycan-binding proteins. To test this, we measured
256 whether teichoic acid depletion affected cell-wall labeling with a fluorescent lectin that specifically binds

257 to the N-acetyl glucosamine moiety of peptidoglycan. We observed an increase in labeling of both Δ*ponA*
258 cells and, to a lesser extent, wild-type cells following pre-treatment with tunicamycin (Fig. S9C). We
259 speculate that teichoic acid depletion in wild-type cells reduces cell wall permeability (Fig. 3A) but
260 increases lectin binding because PBP1 is membrane-bound and would therefore only fill pores near the
261 internal surface of the cell wall, leaving teichoic acid-less peptidoglycan on the outer surface exposed.

262

263 Our model that Rod complexes require a pore-less cell wall as their substrate made the prediction that
264 removing teichoic acids from Δ*ponA* cells by perfusing them with PBS-suspended GlpQ, which arrests cell
265 growth and leads to a permeable cell wall, would prevent Rod complex activity and cell growth upon re-
266 immersion in growth media. Consistent with this prediction, Δ*ponA* cells were unable to recover from
267 teichoic acid digestion but did not lyse upon re-immersion in growth media (Fig. 3D), whereas most wild-
268 type cells recovered (Δ*ponA*: 7% ± 2% recovered. Wild-type: 66% ± 2% recovered. Recovery counted as
269 reaching half the initial, unperturbed growth rate. Error is s.e.m.; Fig. 3E). Furthermore, wild-type cells
270 that resumed growth did so as rods and recovered Rod complex activity (Fig. 3Ei,iii), while cells that did
271 not recover showed no Rod complex motion (Fig. 3Eii,iv, S10A-D). Rod complex activity and cell growth of
272 both wild-type and Δ*ponA* cells recovered fully from incubation in PBS alone (Wild-type: 94% ± 1%
273 recovered growth. Δ*ponA*: 81% ± 2% recovered growth. Error is s.e.m.; Fig. S10E-G, S11A,B). This
274 correlation between pores, Rod complex activity and PBP1 is strong evidence that the Rod complexes
275 cannot add peptidoglycan to a porous cell wall. However, since GlpQ-treatment of wild-type cells does
276 not induce pores (Fig. 3C) but partially inhibits growth recovery (Fig. 3E), teichoic acid digestion must
277 additionally inhibit Rod complexes via a mechanism independent of pores, at least of those that are
278 detected by the mNeonGreen probe. We speculate that this results from the effect of spatially
279 heterogeneous peptidoglycan synthesis by PBP1 on Rod complexes (*Discussion*).

280

281 We reasoned that if pores in the cell wall inhibit Rod complex activity upon teichoic acid removal, then
282 shrinking these pores would activate Rod complexes, thereby promoting cell growth recovery after GlpQ
283 treatment. We tested this prediction by coupling the re-immersion of cells in rich media following GlpQ
284 treatment to a 500 mM hyperosmotic shock that physically contracted the cell wall[59]. To ensure that any
285 cell growth recovery resulted directly from cell wall contraction and not from PBP1 activity, we performed
286 this experiment in Δ*ponA* cells that are otherwise unable to grow following teichoic acid cleavage.
287 Consistent with our hypothesis, we found that hyperosmotic shock led to a partial growth recovery after
288 teichoic acid removal even in the absence of PBP1 (60% ± 2% recovered. Error is s.e.m.; Fig. 3F, S11C).

289

290 Finally, we sought to visualize the effect of teichoic acid depletion on the cell wall. Previously, atomic force
291 microscopy explicitly aimed at resolving peptidoglycan structure did not resolve a difference between
292 isolated cell wall sacculi before and after hydrofluoric acid treatment to remove teichoic acids[60].
293 Therefore, we used transmission electron microscopy to examine the effect of teichoic acid depletion on
294 cell wall ultrastructure. To do this, we performed high pressure freeze-substitution staining on chemically
295 fixed wild-type and Δ*ponA* cells that had been grown either in LB alone or that had been treated for 30
296 min with tunicamycin (*Methods*). We observed significant cell wall degradation of Δ*ponA* tunicamycin-
297 treated cell walls, visible both as general thinning of the cell wall relative to untreated cells, and as
298 localized regions of lower density within the wall (Fig. 3G, S12A). Neither phenomenon was present in
299 wild-type cells treated with tunicamycin (Fig. 3H, S12B). We also observed an electron-dense band on the
300 inner face of the untreated cell wall that is absent in tunicamycin-treated cells (Fig. 3H), consistent with
301 prior observations of a granular, teichoic acid-dependent layer supporting the Gram-positive periplasm in
302 *Streptococcus pneumoniae*[61]. Although this technique is incapable of resolving the nanoscale pores

303 detected by our permeability assays, these findings are consistent with the conclusion that PBP1 fills pores
304 within the cell wall during teichoic acid depletion, and that in Δ*ponA* cells, teichoic acid depletion causes
305 significant cell wall degradation, leading to a loss of Rod complex activity.

306

307 **Rod complex inhibition and shape loss occur during teichoic acid depletion in hydrolase mutants**

308 We finally questioned whether the cell wall degradation that occurs upon teichoic acid depletion in *ΔponA*
309 cells (Fig. 3A,B,G, S12A) depends on specific peptidoglycan hydrolases. Although *Bacillus subtilis* encodes
310 up to 42 putative hydrolases, cell growth can be sustained by either of two synthetically lethal D,L
311 endopeptidases: CwlO or LytE[8]. Furthermore, teichoic acid depletion significantly increases SigI-
312 dependent *lytE* expression[54]. Therefore, we measured the growth rate and width dynamics of Δ*cwlO* and
313 Δ*lytE* cells upon tunicamycin treatment, in the presence or absence of PBP1, and found that the initial
314 phases of these dynamics were identical to those of the respective background strains possessing both
315 hydrolases (Fig. S13A-D). Additionally, upon tunicamycin treatment, Rod complex activity decreased in
316 both hydrolase mutants, as it did in wild-type cells (Fig. S13E-J). Strikingly, at long times after either
317 tunicamycin treatment (Fig. S14A), or transcriptional inhibition of *tagO* (Fig. S14B), Δ*lytE* cells failed to
318 grow. This means that *lytE,* like *ponA,* is essential during teichoic acid depletion.

319

320 **Discussion**

321 Our data support a model in which teichoic acids occlude nanoscopic pores in peptidoglycan (Fig. 4A,B)
322 and prevent them from growing, which promotes rod shape by inhibiting PBP1 and enabling Rod complex
323 activity. According to this model, in wild-type cells teichoic acids limit PBP1's access to natural pores within
324 peptidoglycan by "filling" them and/or by "lining" the inner face of the cell wall (Fig. 4C). When teichoic

325 acids are depleted, PBP1's intrinsically disordered domain rapidly senses the pores, leading to an increase
326 in the relative amount of peptidoglycan that PBP1 synthesizes (Fig. 2D); we find it likely that the anionic
327 teichoic acids exclude the anionic intrinsically disordered domain from pores in the cell wall through
328 polymer-polymer repulsion, similar to the forces that govern macromolecular crowding[62]. Teichoic acid
329 depletion also leads to an increase in PBP1 abundance (Fig. S6F-I) via an unknown mechanism. PBP1 is
330 therefore the essential peptidoglycan synthase driving amorphous growth. This amorphous growth
331 manifests gradually, via an intermediate "dumbbell" morphology that may reflect local reinforcement of
332 the cell wall by septa[5] (Fig. S15). Our model explains prior observations that Rod complexes become
333 dispensable during teichoic acid depletion[63].

334

335 At slightly longer times, teichoic acid depletion leads to decreased activity of Rod complexes (Fig. 1C).
336 According to our model, this occurs in wild-type cells because increased PBP1-mediated synthesis inhibits
337 Rod complex activity by reducing the lipid II pool. Reducing lipid II synthesis is known to inhibit Rod
338 complex activity in both fast and slow growth conditions[25], and we observed a reduction of Rod complex
339 activity during teichoic acid depletion in both conditions (Fig. 1C, S3G-I). We speculate, however, that the
340 heterogenous spatial distribution of PBP1-synthesized peptidoglycan upon teichoic acid depletion
341 amplifies the inhibition of Rod complexes because one function of PBP1 in untreated cells is to contribute
342 to a dense, homogeneous "lawn" of acceptor peptides. This hypothesis is consistent with the impaired
343 Rod complex function of Δ*ponA* mutants during vegetative growth[64], which we suppressed with
344 supplemental magnesium (*Methods*). Localized PBP1 synthesis could inhibit Rod complexes if the latter
345 could only cross-link efficiently to recently synthesized peptidoglycan (or peptidoglycan that is still being
346 synthesized) due to either spatial or biochemical maturation of acceptor peptides (e.g. proximity to the
347 plasma membrane). The heterogeneity of immature peptidoglycan would not inhibit PBP1 since it is not
348 spatially processive, and can therefore cross-link to its own products.

349

350 In the absence of PBP1, teichoic acid depletion causes the simultaneous formation of nanoscopic pores in
351 the cell wall (Fig. 3C) and the eventual arrest of Rod complexes (Fig. 2D,3D). According to our model, the
352 pores exposed by teichoic acid depletion enlarge through hydrolysis without repair by PBP1 (Fig. 3A,B,
353 4A). When the pores become too large, the density of peptide acceptors becomes so low that Rod
354 complexes arrest for the same reason that pharmacological inhibition of Class B PBP transpeptidation
355 arrests Rod complexes[19–21]. Conversely, when these pores are contracted, Rod complex activity can
356 recover (Fig. 3F). The delay in Rod complex arrest that we observed in Δ*ponA* mutants compared to that
357 in wild-type cells is consistent with competitive inhibition of Rod complexes by PBP1.

358

359 Our model accounts for why Rod complex activity partially recovers at late times after teichoic acid
360 depletion, and in Δ*tagO* mutants. The transition from thin rods, to wide rods, to amorphous spheroids
361 directly lowers the growth rate and the surface area-to-volume ratio of the cells, which is expected to
362 increase lipid II levels by lowering the fraction of metabolic flux, per unit cell volume, needed for cell wall
363 expansion. Rod complexes therefore become partially active again, but not at a high enough level to
364 confer rod shape since PBP1 is constitutively de-inhibited and still directs peptidoglycan synthesis to
365 nascent, teichoic acid-less pores.

366

367 In addition to cell wall synthesis, teichoic acids also influence peptidoglycan hydrolysis during cell growth,
368 both directly and indirectly[36–39,54]. We found that *lytE* becomes essential during teichoic acid depletion for
369 cells grown in LB, meaning that stable, amorphous teichoic acid-less growth is driven by PBP1 and LytE.
370 However, deletion of *cwlO* or *lytE* had no effect on the growth, shape and Rod complex dynamics at early
371 times after teichoic acid depletion, indicating that teichoic acids do not differentially regulate these two

372 enzymes. Whether this conditional essentiality of *lytE* arises due to CwlO becoming inactive at long times
373 following teichoic acid depletion will be the subject of further study. Our data suggests that in addition to
374 directly occluding PBP1 from pores, teichoic acids also inhibit peptidoglycan hydrolysis during incubation
375 in PBS (autolysis), potentially through inhibition of LytC and LytD[56]. Teichoic acids' inhibition of hydrolysis
376 could therefore underlie our observation that GlpQ-mediated digestion of teichoic acids partially prevents
377 recovery of wild-type cells even though PBP1 activity prevents the formation of large pores (Fig. 3E). For
378 example, runaway PBP1 activity and hydrolysis during GlpQ treatment could create an irreversibly altered
379 cell wall incapable of supporting Rod complex activity.

380

381 *B. subtilis* cells depleted for wall teichoic acids often fail to separate and show aberrantly thick septa[5,6].
382 Our data is consistent with increased PBP1-mediated synthesis contributing to septal peptidoglycan
383 synthesis since Δ*ponA* cells show reduced septal HADA labeling relative to wild type cells during
384 tunicamycin treatment (Fig. 1D). However, since teichoic acid-depleted cells that are forced to maintain
385 rod shape through confinement grow and divide faster than their spherical counterparts[6], the loss of rod
386 shape clearly contributes substantially to this division defect.

387

388 In sum, wall teichoic acids are critical regulators of rod-shaped morphogenesis in Gram-positive bacteria
389 since they coordinately influence both modes of peptidoglycan synthesis as well as its hydrolysis. Our
390 study resolves the longstanding question of how teichoic acids promote rod-shape without directly
391 contributing to cell wall anisotropy. Furthermore, we establish a direct link between the molecular
392 structure of the cell wall and anisotropic cell wall synthesis, identifying the cell wall as a critical
393 autoregulatory factor of its own synthesis, rather than a passive substrate.

394

395 **References**

396 1. Dion, M. F. *et al.* Bacillus subtilis cell diameter is determined by the opposing actions of two distinct
397 cell wall synthetic systems. *Nature Microbiology* **4**, 1294–1305 (2019).
398 2. Garner, E. C. Toward a Mechanistic Understanding of Bacterial Rod Shape Formation and
399 Regulation. *Annual Review of Cell and Developmental Biology* **37**, null (2021).
400 3. Young, K. D. The Selective Value of Bacterial Shape. *Microbiology and Molecular Biology Reviews* **70**,
401 660–703 (2006).
402 4. Cho, H. *et al.* Bacterial cell wall biogenesis is mediated by SEDS and PBP polymerase families
403 functioning semi-autonomously. *Nat Microbiol* **1**, 1–8 (2016).
404 5. D'Elia, M. A., Millar, K. E., Beveridge, T. J. & Brown, E. D. Wall Teichoic Acid Polymers Are
405 Dispensable for Cell Viability in Bacillus subtilis. *Journal of Bacteriology* **188**, 8313–8316 (2006).
406 6. Hussain, S. *et al.* MreB filaments align along greatest principal membrane curvature to orient cell
407 wall synthesis. *eLife* **7**, e32471 (2018).
408 7. Schirner, K. *et al.* Lipid-linked cell wall precursors regulate membrane association of bacterial actin
409 MreB. *Nature Chemical Biology* **11**, 38–45 (2015).
410 8. Wilson, S. A., Tank, R. K. J., Hobbs, J. K., Foster, S. J. & Garner, E. C. An exhaustive multiple knockout
411 approach to understanding cell wall hydrolase function in Bacillus subtilis. *mBio* **14**, e01760-23
412 (2023).
413 9. Rojas, E., Theriot, J. A. & Huang, K. C. Response of Escherichia coli growth rate to osmotic shock.
414 *PNAS* **111**, 7807–7812 (2014).
415 10. Goldman, W. E., Klapper, D. G. & Baseman, J. B. Detection, isolation, and analysis of a released
416 Bordetella pertussis product toxic to cultured tracheal cells. *Infection and Immunity* **36**, 782–794
417 (1982).

418 11. Sassine, J. *et al.* Functional redundancy of division specific penicillin-binding proteins in Bacillus
419 subtilis. *Molecular Microbiology* **106**, 304–318 (2017).
420 12. Barber, F., Min, J., Murray, A. W. & Amir, A. Modeling the impact of single-cell stochasticity and size
421 control on the population growth rate in asymmetrically dividing cells. *PLOS Computational Biology*
422 **17**, e1009080 (2021).
423 13. Barber, F., Ho, P.-Y., Murray, A. W. & Amir, A. Details Matter: Noise and Model Structure Set the
424 Relationship between Cell Size and Cell Cycle Timing. *Frontiers in Cell and Developmental Biology* **5**,
425 (2017).
426 14. Chang, F. & Huang, K. C. How and why cells grow as rods. *BMC Biol* **12**, 54 (2014).
427 15. Armstrong, J. J., Baddiley, J., Buchanan, J. G. & Carss, B. Nucleotides and the Bacterial Cell Wall.
428 *Nature* **181**, 1692–1693 (1958).
429 16. Armstrong, J. J. *et al.* Teichoic Acids from Bacterial Walls: Composition of Teichoic Acids from a
430 Number of Bacterial Walls. *Nature* **184**, 247–248 (1959).
431 17. Boylan, R. J., Mendelson, N. H., Brooks, D. & Young, F. E. Regulation of the Bacterial Cell Wall:
432 Analysis of a Mutant of Bacillus subtilis Defective in Biosynthesis of Teichoic Acid. *Journal of*
433 *Bacteriology* **110**, 281–290 (1972).
434 18. Eugster, M. R. & Loessner, M. J. Wall Teichoic Acids Restrict Access of Bacteriophage Endolysin
435 Ply118, Ply511, and PlyP40 Cell Wall Binding Domains to the Listeria monocytogenes Peptidoglycan.
436 *J Bacteriol* **194**, 6498–6506 (2012).
437 19. Garner, E. C. *et al.* Coupled, Circumferential Motions of the Cell Wall Synthesis Machinery and MreB
438 Filaments in B. subtilis. *Science* **333**, 222–225 (2011).
439 20. van Teeffelen, S. *et al.* The bacterial actin MreB rotates, and rotation depends on cell-wall assembly.
440 *Proceedings of the National Academy of Sciences* **108**, 15822–15827 (2011).

441 21. Domínguez-Escobar, J. *et al.* Processive Movement of MreB-Associated Cell Wall Biosynthetic
442 Complexes in Bacteria. *Science* **333**, 225–228 (2011).
443 22. Carballido-López, R. *et al.* Actin homolog MreBH governs cell morphogenesis by localization of the
444 cell wall hydrolase LytE. *Dev Cell* **11**, 399–409 (2006).
445 23. Daniel, R. A. & Errington, J. Control of cell morphogenesis in bacteria: two distinct ways to make a
446 rod-shaped cell. *Cell* **113**, 767–776 (2003).
447 24. Billaudeau, C. *et al.* Contrasting mechanisms of growth in two model rod-shaped bacteria. *Nature*
448 *Communications* **8**, 15370 (2017).
449 25. Sun, Y., Hürlimann, S. & Garner, E. Growth rate is modulated by monitoring cell wall precursors in
450 Bacillus subtilis. *Nat Microbiol* **8**, 469–480 (2023).
451 26. Meeske, A. J. *et al.* SEDS proteins are a widespread family of bacterial cell wall polymerases. *Nature*
452 **537**, 634–638 (2016).
453 27. Wei, Y., Havasy, T., McPherson, D. C. & Popham, D. L. Rod Shape Determination by the Bacillus
454 subtilis Class B Penicillin-Binding Proteins Encoded by pbpA and pbpH. *Journal of Bacteriology* **185**,
455 4717–4726 (2003).
456 28. McPherson, D. C. & Popham, D. L. Peptidoglycan Synthesis in the Absence of Class A Penicillin-
457 Binding Proteins in Bacillus subtilis. *Journal of Bacteriology* **185**, 1423–1431 (2003).
458 29. Brunet, Y. R., Habib, C., Brogan, A. P., Artzi, L. & Rudner, D. Z. Intrinsically disordered protein regions
459 are required for cell wall homeostasis in Bacillus subtilis. *Genes Dev* **36**, 970–984 (2022).
460 30. Brown, S. *et al.* Methicillin resistance in Staphylococcus aureus requires glycosylated wall teichoic
461 acids. *Proc Natl Acad Sci U S A* **109**, 18909–18914 (2012).
462 31. Campbell, J. *et al.* Synthetic Lethal Compound Combinations Reveal a Fundamental Connection
463 between Wall Teichoic Acid and Peptidoglycan Biosyntheses in Staphylococcus aureus. *ACS Chem.*
464 *Biol.* **6**, 106–116 (2011).

465 32. Farha, M. A. *et al.* Inhibition of WTA Synthesis Blocks the Cooperative Action of PBPs and Sensitizes
466 MRSA to beta-Lactams. *ACS Chem. Biol.* **8**, 226–233 (2013).
467 33. Lu, Y. *et al.* Modulation of MRSA virulence gene expression by the wall teichoic acid enzyme TarO.
468 *Nat Commun* **14**, 1594 (2023).
469 34. Thomas, K. J. & Rice, C. V. Equilibrium binding behavior of magnesium to wall teichoic acid.
470 *Biochimica et Biophysica Acta (BBA) - Biomembranes* **1848**, 1981–1987 (2015).
471 35. Wecke, J., Madela, K. & Fischer, W. The absence of D-alanine from lipoteichoic acid and wall teichoic
472 acid alters surface charge, enhances autolysis and increases susceptibility to methicillin in Bacillus
473 subtilis. *Microbiology (Reading)* **143**, 2953–2960 (1997).
474 36. Bonnet, J. *et al.* Nascent teichoic acids insertion into the cell wall directs the localization and activity
475 of the major pneumococcal autolysin LytA. *The Cell Surface* **2**, 24–37 (2018).
476 37. Wecke, J., Perego, M. & Fischer, W. d-Alanine Deprivation of Bacillus subtilis Teichoic Acids Is
477 without Effect on Cell Growth and Morphology But Affects the Autolytic Activity. *Microbial Drug*
478 *Resistance* **2**, 123–129 (1996).
479 38. Flores-Kim, J., Dobihal, G. S., Fenton, A., Rudner, D. Z. & Bernhardt, T. G. A switch in surface polymer
480 biogenesis triggers growth-phase-dependent and antibiotic-induced bacteriolysis. *eLife* **8**, e44912
481 (2019).
482 39. Flores-Kim, J., Dobihal, G. S., Bernhardt, T. G. & Rudner, D. Z. WhyD tailors surface polymers to
483 prevent premature bacteriolysis and direct cell elongation in Streptococcus pneumoniae. *eLife* **11**,
484 e76392 (2022).
485 40. Atilano, M. L. *et al.* Teichoic acids are temporal and spatial regulators of peptidoglycan cross-linking
486 in Staphylococcus aureus. *PNAS* **107**, 18991–18996 (2010).

487 41. Formstone, A., Carballido-López, R., Noirot, P., Errington, J. & Scheffers, D.-J. Localization and
488 Interactions of Teichoic Acid Synthetic Enzymes in Bacillus subtilis. *Journal of Bacteriology* **190**,
489 1812–1821 (2008).
490 42. Koyano, Y., Okajima, K., Mihara, M. & Yamamoto, H. Visualization of Wall Teichoic Acid Decoration
491 in Bacillus subtilis. *Journal of Bacteriology* **0**, e00066-23 (2023).
492 43. Bonnet, J. *et al.* One-Pot Two-Step Metabolic Labeling of Teichoic Acids and Direct Labeling of
493 Peptidoglycan Reveals Tight Coordination of Both Polymers Inserted into Pneumococcus Cell Wall.
494 *ACS Chem. Biol.* **13**, 2010–2015 (2018).
495 44. Bracha, R. & Glaser, L. An intermediate in teichoic acid biosynthesis. *Biochemical and Biophysical*
496 *Research Communications* **72**, 1091–1098 (1976).
497 45. Hancock, I. C., Wiseman, G. & Baddiley, J. Biosynthesis of the unit that links teichoic acid to the
498 bacterial wall: Inhibition by tunicamycin. *FEBS Letters* **69**, 75–80 (1976).
499 46. Mirouze, N., Ferret, C., Cornilleau, C. & Carballido-López, R. Antibiotic sensitivity reveals that wall
500 teichoic acids mediate DNA binding during competence in Bacillus subtilis. *Nat Commun* **9**, 5072
501 (2018).
502 47. Hsu, Y.-P. *et al.* Fluorogenic d -amino acids enable real-time monitoring of peptidoglycan
503 biosynthesis and high-throughput transpeptidation assays. *Nature Chemistry* **11**, 335–341 (2019).
504 48. Lupoli, T. J. *et al.* Transpeptidase-Mediated Incorporation of d-Amino Acids into Bacterial
505 Peptidoglycan. *J. Am. Chem. Soc.* **133**, 10748–10751 (2011).
506 49. Liechti, G. W. *et al.* A new metabolic cell-wall labelling method reveals peptidoglycan in Chlamydia
507 trachomatis. *Nature* **506**, 507–510 (2014).
508 50. Atrih, A., Bacher, G., Allmaier, G., Williamson, M. P. & Foster, S. J. Analysis of peptidoglycan
509 structure from vegetative cells of Bacillus subtilis 168 and role of PBP 5 in peptidoglycan maturation.
510 *J Bacteriol* **181**, 3956–3966 (1999).

511 51. Sauvage, E. & Terrak, M. Glycosyltransferases and Transpeptidases/Penicillin-Binding Proteins:
512 Valuable Targets for New Antibacterials. *Antibiotics* **5**, 12 (2016).
513 52. Bertsche, U., Breukink, E., Kast, T. & Vollmer, W. *In Vitro* Murein (Peptidoglycan) Synthesis by
514 Dimers of the Bifunctional Transglycosylase-Transpeptidase PBP1B from *Escherichia coli**. *Journal of*
515 *Biological Chemistry* **280**, 38096–38101 (2005).
516 53. Sharifzadeh, S., Dempwolff, F., Kearns, D. B. & Carlson, E. E. Harnessing β-Lactam Antibiotics for
517 Illumination of the Activity of Penicillin-Binding Proteins in Bacillus subtilis. *ACS Chem. Biol.* **15**,
518 1242–1251 (2020).
519 54. Kasahara, J. *et al.* Teichoic Acid Polymers Affect Expression and Localization of dl-Endopeptidase
520 LytE Required for Lateral Cell Wall Hydrolysis in Bacillus subtilis. *Journal of Bacteriology* **198**, 1585–
521 1594 (2016).
522 55. Halladin, D. K. *et al.* Entropy-driven translocation of disordered proteins through the Gram-positive
523 bacterial cell wall. *Nat Microbiol* **6**, 1055–1065 (2021).
524 56. Akbary, Z. *et al.* Peptidoglycan turnover promotes active transport of protein through the bacterial
525 cell wall. 2025.09.12.675941 Preprint at https://doi.org/10.1101/2025.09.12.675941 (2025).
526 57. Erickson, H. P. Size and Shape of Protein Molecules at the Nanometer Level Determined by
527 Sedimentation, Gel Filtration, and Electron Microscopy. *Biol Proced Online* **11**, 32–51 (2009).
528 58. Myers, C. L. *et al.* Identification of Two Phosphate Starvation-induced Wall Teichoic Acid Hydrolases
529 Provides First Insights into the Degradative Pathway of a Key Bacterial Cell Wall Component*.
530 *Journal of Biological Chemistry* **291**, 26066–26082 (2016).
531 59. Bardetti, P., Barber, F. & Rojas, E. R. Non-linear stress-softening of the bacterial cell wall confers cell
532 shape homeostasis. 2024.09.03.611099 Preprint at https://doi.org/10.1101/2024.09.03.611099
533 (2024).

60. Pasquina-Lemonche, L. *et al.* The architecture of the Gram-positive bacterial cell wall. *Nature* **582**, 294–297 (2020).

61. Nguyen, M. *et al.* Teichoic acids in the periplasm and cell envelope of Streptococcus pneumoniae. *eLife* **14**, RP105132 (2025).

62. Delarue, M. *et al.* mTORC1 Controls Phase Separation and the Biophysical Properties of the Cytoplasm by Tuning Crowding. *Cell* **174**, 338-349.e20 (2018).

63. Kawai, Y. *et al.* A widespread family of bacterial cell wall assembly proteins. *The EMBO Journal* **30**, 4931–4941 (2011).

64. Murray, T., Popham, D. L. & Setlow, P. Bacillus subtilis Cells Lacking Penicillin-Binding Protein 1 Require Increased Levels of Divalent Cations for Growth. *J Bacteriol* **180**, 4555–4563 (1998).

Figures

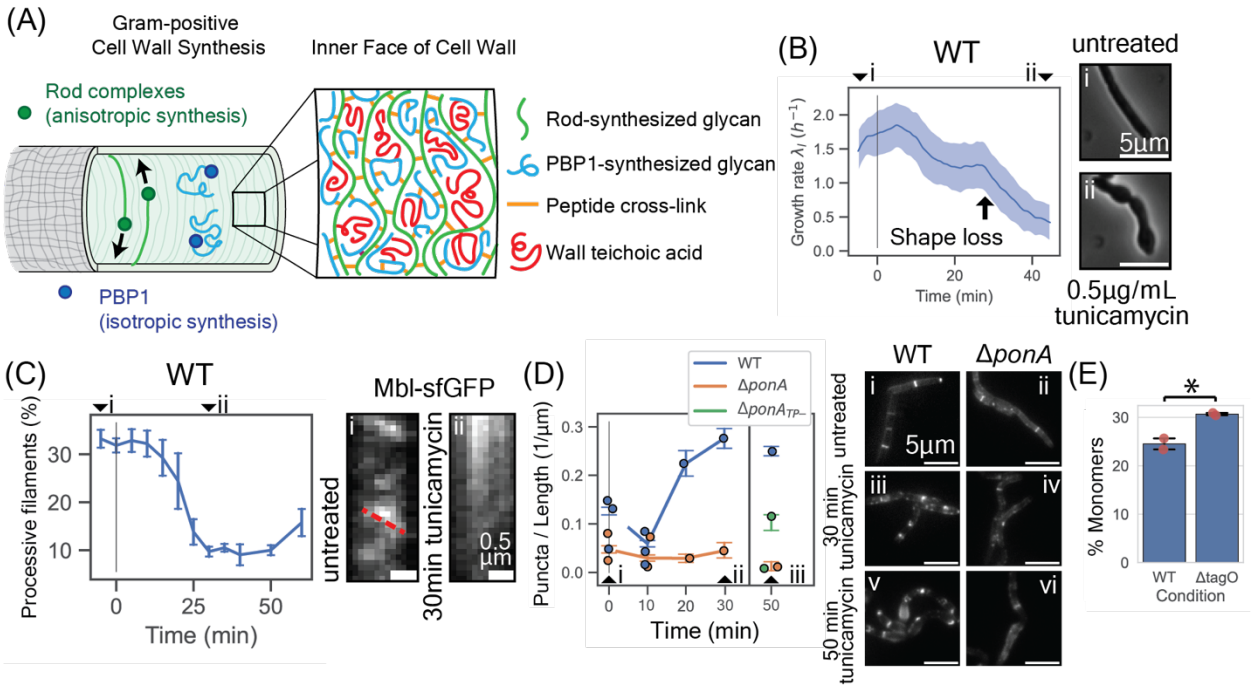

Fig. 1: Inhibiting wall teichoic acid synthesis decreases Rod complex activity prior to cell shape loss. (A) Schematic of Gram-positive cell wall synthesis. **(B)** Cell length growth rate $\lambda_l = \frac{1}{l}\frac{dl}{dt}$ for wild-type cells

550 during 0.5 μg/mL tunicamycin treatment. Blue line shows smoothed population median, error bars show
551 standard deviation. Data shown for 2,048 discrete cell tracks from 3 biological replicates. Inset:
552 micrographs taken (i) before and (ii) after 45 min tunicamycin treatment. Scale bars 5 μm. **(C)** Time course
553 for the percentage of processive Mbl filaments during 0.5 μg/mL tunicamycin treatment. Error bars show
554 95% confidence intervals across biological replicates (bootstrap analysis). Analysis performed on 62,901
555 discrete filament tracks from 4 biological replicates. Inset shows representative fluorescent kymographs
556 of Mbl motion across the cell waist in (i) LB and (ii) after 30 min tunicamycin treatment. Red dotted line
557 follows a processive Mbl filament. Scale bars 1 μm. **(D)** Mean fluorescent puncta per unit cell length for
558 wild-type, Δ*ponA* and $ponA_{TP-}$cells during tunicamycin treatment, labeled with fluorescent D-amino acids.
559 Error bars show 95% confidence intervals. Analysis performed over 2,017 segmentations from 4 biological
560 replicates (wild-type), 857 segmentations from 3 biological replicates (Δ*ponA*) and 257 cells from 2
561 biological replicates ($ponA_{TP-}$). All timepoints show statistical significance for difference in mean between
562 cell types (Student's T-test, P<0.01). Dots show individual replicates. Measurements at 50 min tunicamycin
563 treatment used a lower exposure time so are plotted separately. Inset shows micrographs of (i,iii,v) wild-
564 type and (ii,iv,vi) Δ*ponA* cells at (i,ii) 0 min, (iii,iv) 30 min, and (v,vi) 50 min of treatment. Micrographs are
565 identically saturated across cell types. Scale bars 5 μm. **(E)** Percentage of peptidoglycan subunits in
566 monomers, measured by HPLC (*Methods*). Two biological replicates per strain. Mean values calculated
567 across biological replicates. Error bars show 95% confidence intervals. Individual datapoints shown in red.
568 Statistical significance calculated using Student's T-test, P<0.05.

569

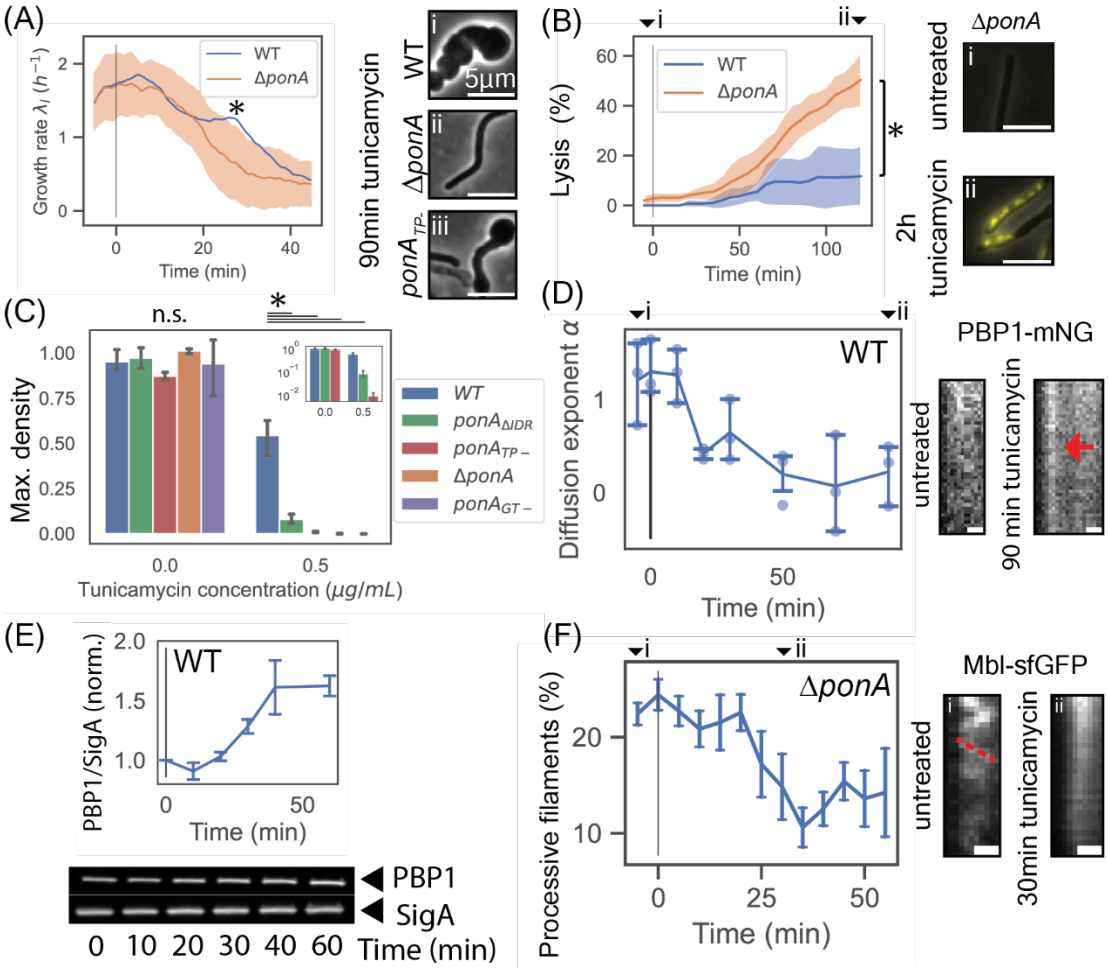

Figure 2: PBP1 is required for growth during wall teichoic acid synthesis inhibition. (A) Cell length growth rate $\lambda_l = \frac{1}{l}\frac{dl}{dt}$ for Δ*ponA* cells during 0.5 µg/mL tunicamycin treatment. Orange line shows smoothed population median, error bars show standard deviation. Analysis performed over 629 discrete cell tracks from 5 biological replicates. Blue line reproduces wild-type data from Fig. 1A. Statistical significance calculated between cell types at 25 min tunicamycin exposure using Student's T-test, P<0.01. Inset: micrographs showing (i) wild-type, (ii) Δ*ponA* and (iii) *ponA*$_{TP-}$ cells following 90 min treatment with 0.5 µg/mL tunicamycin. Scale bars 5 µm. **(B)** Percentage of membrane-disrupted cells following tunicamycin exposure, measured by propidium iodide staining. Solid line shows mean across all fields of view. Error bars show standard deviation of the same. Analysis performed over 1,098 cells from three biological replicates (Δ*ponA*) and 1,105 cells from two biological replicates (wild-type). Statistical significance calculated for final timepoint using Student's T-test, P<0.01. Inset: micrographs of *ΔponA* cells (i) before and (ii) after 2 h tunicamycin treatment. Phase images overlaid with propidium iodide stain. Scale bars 5μm. **(C)** Maximum OD (optical density) for wild-type, *ponA*$_{ΔIDR}$ (expressing PBP1 without its intrinsically

584 disordered region), *ponA*$_{TP-}$ (expressing PBP1 with an inactive transpeptidase domain), Δ*ponA* and *ponA*$_{GT-}$
585 (inducibly expressing PBP1 with an inactive glycosyltransferase domain) with and without a low dose of
586 tunicamycin, grown in bulk culture. Data shown from one representative biological replicate out of three,
587 with four technical replicates per biological replicate. Error bars show 95% confidence intervals based on
588 bootstrap analysis. Inset: same data for WT, *ponA*$_{\Delta IDR}$ and *ponA*$_{TP-}$ cells, plotted on log-scale. Statistical
589 significance tested with one-way ANOVA followed by Tukey's HSD post-hoc test for groups with and
590 without tunicamycin, P<0.01. **(D)** Diffusion exponent α for PBP1 puncta during a time course of
591 tunicamycin treatment (*Methods*). $\alpha = 1$: diffusive, $\alpha < 1$: sub-diffusive. Inset: kymographs of PBP1-
592 mNeonGreen motion for (i) untreated and (ii) 90 min tunicamycin-treated cells. Red arrow points to a
593 static PBP1-mNeonGreen spot during tunicamycin treatment. Total time: 4 s. **(E)** Western blot analysis of
594 PBP1 levels during 0.5μg/mL tunicamycin treatment. Bottom: Western blot bands for PBP1-FLAG and
595 identically loaded SigA control. Loading volumes normalized based on OD600 readings. Top:
596 Quantification of PBP1 staining, normalized by SigA stain and measured relative to values at 0min
597 tunicamycin treatment. Two biological replicates. Error bars show standard error of the mean. **(F)**
598 Percentage of processive Mbl-sfGFP filaments during tunicamycin time course of Δ*ponA* cells. Error bars
599 show 95% confidence intervals across biological replicates based on bootstrap analysis. Analysis
600 performed on 40,793 discrete filament tracks from three biological replicates.

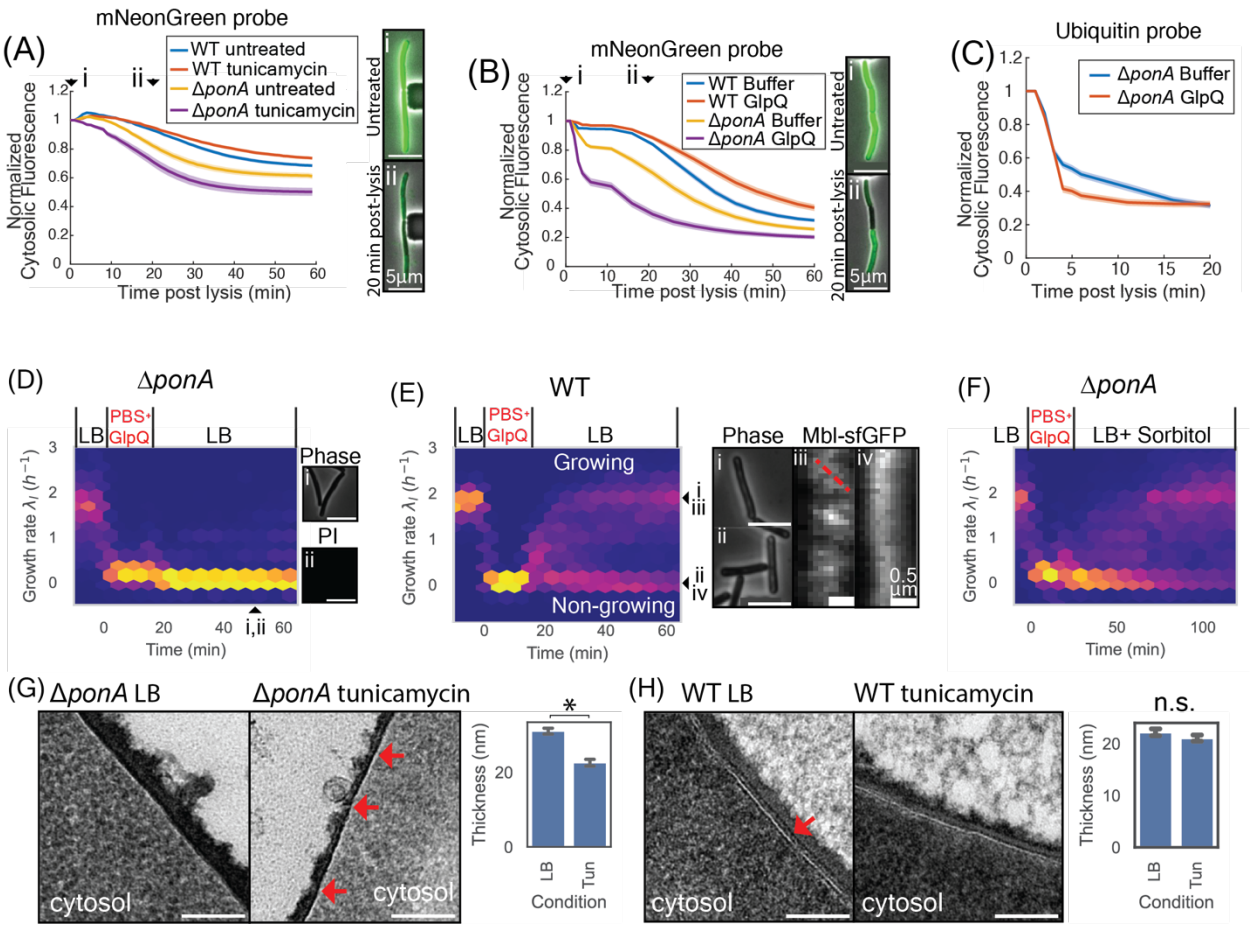

Figure 3: PBP1 fills pores that are exposed upon wall teichoic acid removal, conferring growth. (A) mNeonGreen diffusion out of cells with disrupted membranes following a 10 min (wild-type) or 20 min (Δ*ponA*) incubation with LB supplemented with tunicamycin or with LB alone. Solid lines show population average, error bars show standard error of the mean. Wild-type untreated: 87 cells, 4 biological replicates. Wild-type tunicamycin: 139 cells, 3 biological replicates. Δ*ponA* untreated: 53 cells, 3 biological replicates. Δ*ponA* tunicamycin: 35 cells, 3 biological replicates. Inset: micrographs showing cellular fluorescence of tunicamycin-treated Δ*ponA* cells (i) before and (ii) 20 min after cell lysis. Scale bars 5 μm. **(B)** mNeonGreen diffusion out of lysed wild-type and Δ*ponA* cells following a 15-minute live-cell incubation with PBS supplemented with either 40 µM GlpQ in Buffer A or with Buffer A alone. Wild-type Buffer: 121 cells, 1 biological replicate. Wild-type GlpQ: 90 cells, 1 biological replicate. Δ*ponA* Buffer: 85 cells, 3 biological replicates. Δ*ponA* GlpQ: 108 cells, 3 biological replicates. Inset: micrographs showing cellular fluorescence of GlpQ-treated Δ*ponA* cells (i) before and (ii) 20 min after cell lysis. Scale bars 5μm. **(C)** Ubiquitin-FlAsH diffusion out of lysed Δ*ponA* cells following a 2 min incubation with PBS + 5% N-lauroylsarcosine supplemented with either 40 µM GlpQ or the equivalent volume of Buffer A. **(D)** Heat map showing growth

616 rate $\lambda_l = \frac{1}{l}\frac{dl}{dt}$ of Δ*ponA* cells following a 15 min incubation with 10μM native GlpQ (1,816 discrete tracks,
617 3 biological replicates). Heat map intensity is proportional to the number of cells with a given growth rate
618 at a given time, normalized across the total number of cells tracked at each timepoint. Inset: lack of
619 propidium iodide staining for Δ*ponA* cells 50 min after GlpQ incubation. (i) Phase contrast. (ii) Propidium
620 iodide stain. For positive stain, see Fig. 2B ii. Scale bars 5μm. **(E)** Same as (D) for wild-type cells (3,236
621 discrete tracks, four biological relicates). Inset: (i-ii) cell micrographs of (i) growing and (ii) non-growing
622 cells, and (iii-iv) kymographs of (iii) growing and (iv) non-growing cells, following the exit from GlpQ
623 treatment. Scale bars 5μm in (i,ii), 0.5 μm in (iii,iv). Red dotted line in (iii) follows a processive Mbl
624 filament. **(F)** Heatmap showing Δ*ponA* cell length growth rate $\lambda_l = \frac{1}{l}\frac{dl}{dt}$ when exit from a 15-minute
625 incubation with 10 μM GlpQ was coupled to a 500 mM hyperosmotic shock (3,036 discrete cell tracks, 3
626 biological replicates). **(G-H)** Transmission electron micrographs showing the sidewall of exponentially
627 growing cells grown in either LB or LB supplemented with 0.5 μg/mL tunicamycin for 30 min. Scale bars
628 100 nm. **(G)** Δ*ponA* cells. Red arrows in show sites of severe cell wall thinning during tunicamycin
629 treatment. Inset: average wall thickness for the growth conditions shown, calculated for 47 cells (LB) and
630 44 cells (tunicamycin). Statistical significance calculated using Student's T-test, P<0.01. **(H)** Wild-type cells.
631 Red arrow shows electron-dense band on the inner face of the cell wall, absent in tunicamycin-treated
632 cells. Inset: average wall thickness of wild-type cells for the growth conditions shown, calculated for 31
633 cells (LB) and 28 cells (tunicamycin). No statistically significant difference measured between conditions,
634 Student's T-test for P<0.01.

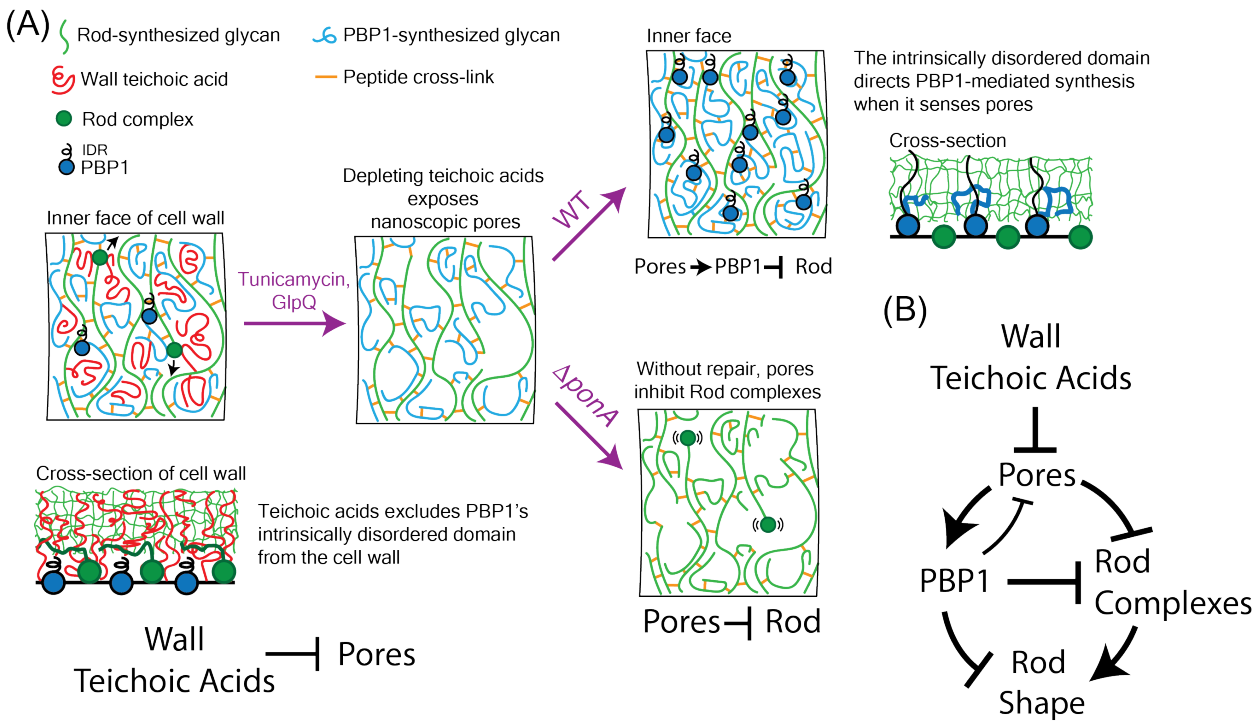

Figure 4: (A) Model illustration. During teichoic acid depletion of wild-type cells, denuded cell wall pores are targeted by PBP1, competitively inhibiting Rod complexes and driving localized peptidoglycan synthesis. This isotropic cell wall synthesis causes decreased growth and loss of cell shape. During teichoic acid depletion of Δ*ponA* cells, denuded cell wall pores directly arrest Rod complex motion through depletion of crosslinking acceptors. **(B)** Schematic of model described in (A).

1 **Methods**

2 **Microscopy**

3 All timelapse microscopy was performed with a Nikon Eclipse Ti2 microscope, outfitted with a
4 photometrics PRIME BSI CMOS camera (Teledyne Photometrics) and a Nikon 100X Plan Apo Phase
5 Contrast objective, NA 1.45. All non-TIRF fluorescence imaging used LED illumination. We conducted all
6 imaging using CellASIC ONIX microfluidic plates (Millipore B04A-03), using standard priming and media
7 exchange protocols. We heated all microscope stage components, CellASIC plates, and objectives to 37°C
8 prior to imaging using a microscope incubator outfitted with a heater. We performed our timelapse phase
9 contrast microscopy using 20s timesteps, monitoring medium exchange using the dye AlexaFluor 647 at
10 a final media concentration of 2.5µg/mL, with CY5 illumination adjusted to avoid any confounding effects
11 of phototoxicity.

12 **Total Internal Reflection Fluorescence (TIRF) Microscopy**

13 All TIRF microscopy was performed with the same Nikon Eclipse Ti2 microscope, using a COHERENT 488nm
14 laser and 100X Plan Apo objective, NA 1.45, with 2s timesteps. We adjusted our laser power, exposure
15 time and TIRF alignment to minimize photobleaching, and used a fresh field of view for each new
16 timepoint to avoid any confounding effects of phototoxicity.

17 **Single Molecule Tracking**

18 We performed single molecule tracking by imaging small fields of view with TIRF microscopy, using a
19 timestep of 90ms, laser power 1% and 40ms camera exposure time. To facilitate the rapid image
20 acquisition, the laser remained on constantly for the 4s acquisition. To facilitate single-molecule
21 resolution, we induced PBP1-mNeonGreen expression at low levels from a heterologous HyperSpank
22 promoter with 10uM IPTG (Isopropyl ß-D-1-thiogalactopyranoside), alongside unperturbed native PBP1

23 expression from the endogenous locus. Note: Videos S8 and S9 were acquired with imaging conditions
24 that visually emphasize the duration of PBP1 puncta during teichoic acid depletion, but that were not used
25 for single-molecule tracking because of their low time-resolution: time step = 500ms, exposure time 50ms,
26 15s time course, 1% laser power. We generated our image file structures for downstream analysis using
27 the ImageJ script tirf_pbp1_processing_v1.ijm. We then performed spot tracking using the python script
28 single_molecule_tracking_v1.py, which detected and tracked filaments as follows: we detected puncta
29 with SciKitImage's bloblog feature, using manually curated thresholds to start each timelapse (that were
30 then preserved within all timelapses acquired using that imaging condition). These thresholds were
31 iteratively reduced throughout each step of a single time course to maintain roughly equivalent levels of
32 spot detection. This allowed us to correct for partial photobleaching of the fluorescent signal. We tracked
33 individual puncta across successive images (all analysed images used a timestep of 90ms) by calculating
34 the minimum distance between all annotated puncta, subject to a maximum displacement threshold of
35 two pixels (equivalent to a linear distance of 186nm based on our magnification and camera size). We
36 then filtered to exclude all tracks with length 2 timepoints or less. Finally, we inferred the diffusion
37 exponents by applying linear regression to log-log plots for the population-averaged mean-squared
38 displacement of individual PBP1 puncta over time.

39 **Cell culture and transformation**

40 Unless otherwise stated, all cell culture was performed with LB media (Luria Broth, Lennox). All *in vivo*
41 imaging and spot-assay experiments were performed with log-phase cultures of OD600≤0.2.
42 Transformations were performed with competent *B. subtilis* cells grown in MC Media + 20mM $MgSO_4$,
43 then plated onto LB agarose plates. All cells were congenic with a PY79 strain background. Strains are
44 tabulated in Table S1. We note that expression of $ponA_{TG}$*-(E115A)* at high levels was toxic to cells, and
45 required media supplementation with 30mM $MgCl_2$. Similarly, our experiments on Rod complex tracking

46 in Δ*ponA* cells were performed with 10mM supplemental $MgCl_2$ to allow us to visualize processive
47 Rod complexes in this strain background.

48

49 **S750 media**

50 We used S750 defined minimal media following a recipe used previously[1]: 1x S750 salts, 1x S750 Metals,
51 1% Glucose, 0.1% Glutamate + distilled H2O to final volume.

52 10x S750 salts: 0.5 M MOPS (adjusted to pH 7.0 with KOH), 100 mM Ammonium Sulfate, 50 mM Potassium
53 Phosphate Monobasic (adjusted to pH 7.0). Filter sterilized.

54 100x S750 Metals: 0.2 M $MgCl_2$, 70 mM $CaCl_2$, 5 mM $MnCl_2$, 0.1 mM $ZnCl_2$, 100 µg/mL Thiamine HCl, 2 mM
55 HCl, 0.5 mM $FeCl_3$, dH_2O to final volume.

56 We performed our S750 experiments by first inoculating overnight S750 cultures from LB plates, then
57 back diluting the following morning into fresh S750 media and allowing these new cultures to grow to
58 exponential phase prior to starting an experiment.

59 **Click Labeling of Peptidoglycan Precursors**

60 We treated exponentially growing cultures with 1mM EDA-DA (ethynyl-D-alanine D-alanine, Fisher
61 Scientific 771410) for 20 min at 37°C. We then washed cell cultures once in PBS, before fixing cells
62 for 20 min on ice in PBS supplemented with 3.6% paraformaldehyde. We labeled the EDA-DA alkyne
63 group with Alexa Fluor 488 Azide (A10266) by following the Invitrogen Click-iT™ Cell Reaction Buffer
64 Kit (Thermo Fisher, C10269), but without supplementing with BSA (to ensure optimal diffusion
65 through the cell wall). We spotted cells onto PBS pads made with 2% agarose and imaged all
66 samples within 18 h of click-labeling. We generated different treatment conditions by inoculating
67 identical, prewarmed tubes of fresh growth media from a single exponentially growing culture. We

68 generated our tunicamycin-treated samples by pre-treating for 10 min with 0.5 μg/mL tunicamycin prior
69 to EDA-DA addition, for a total of 30 min drug exposure. By contrast, we added 50 μg/mL fosfomycin or 1
70 μg/mL vancomycin simultaneous with EDA-DA for a total of 20 min drug exposure.

71 **Protein purification and application**

72 Protein was purified according to the following, previously published method[2]: We incubated cell cultures
73 of bER461 in 500mL LB + 100 ug/mL Ampicillin and 35 ug/mL Chloramphenicol at 37°C with shaking until
74 they reached an OD600 of 0.6-0.8. We then shifted these cultures to 16°C, added IPTG (Isopropyl ß-D-1-
75 thiogalactopyranoside) to a final concentration of 0.5mM, and incubated with shaking for 18h. We
76 centrifuged these cultures at 4°C, resuspended in Buffer A (50 mM Tris-HCl + 200 mM NaCl + 1 mM CaCl2 +
77 1 mM MgCl2, pH 8.0) +25mM Imidazole and lysed by disruption in an Emulsiflex-C5. After disruption, we
78 incubated the supernatant with a column containing HisPur Ni-NTA Resin (ThermoFisher 88221), ran this
79 column over an Imidazole gradient, and visualized samples via SDS-PAGE with stain-free labeling (BioRad
80 1610183). We pooled column elutions containing high protein concentrations, performed dialysis at 4°C
81 overnight in Buffer A, concentrated our samples with Amicon Ultra Centrifugal Filters (10KDa molecular
82 weight cutoff), and flash-froze single-use aliquots with liquid nitrogen for storage at -80°C. We calculated
83 our protein concentration by nanodrop.

84 The Gram-positive cell wall imposes a substantial diffusion barrier to molecules above 15kDa[3]. At 30.1kDa,
85 GlpQ exceeds this limit substantially, rendering it necessary to partially degrade the cell wall to allow GlpQ
86 access to its target substrates. We accomplished this by performing all GlpQ incubations in PBS lacking
87 divalent cations for the times listed. This incubation simultaneously arrested peptidoglycan synthesis and
88 induced autolysis (cell wall degradation) by the cells' native autolysins. We made the PBS used to perform
89 these incubations according to the following recipe[4] (10X PBS, 1L): 80g NaCl, 2g KCl, 14.4g Na_2HPO_4, 2.4g
90 KH_2PO_4. Adjust pH to 7.4 with HCl.

91 ***In vivo* bocillin labeling**

92 We grew cell cultures to early log-phase, back diluted into prewarmed LB to create multiple identical, log-
93 phase samples, and added tunicamycin (MP Biomedical 0215002805 and Cell Signaling Technology 12819)
94 to each sample at successive time intervals of 10 min, to a final concentration of 0.5µg/mL. Prior to lysis,
95 we treated all cultures with bocillin-FL (Invitrogen, B13233) simultaneously to a final concentration of
96 1µg/mL, incubated for 2 min, then pelleted cells for cell lysate extraction. We treated cell pellets with lysis
97 buffer (20mM Tris pH 7.5, 1mM EDTA, 10mM $MgCl_2$, 1mg/mL Lysozyme, 1mM PMSF, 10ug/mL DNAse I,
98 100ug/mL RNAse A). We added fresh Lysozyme, PMSF, DNAse I and RNAse A to a lysis buffer stock for
99 each preparation. We then visualized cell lysates via SDS-PAGE (FastCast 10% Acrylamide, Bio-Rad
100 1610183) using a Cytiva Amersham Typhoon fluorescent imager.

101 **Wall teichoic acid measurement by flow cytometry**

102 We grew cell cultures to log-phase (OD600=0.1-0.2), then took two samples from a single cell culture,
103 washed 1X in PBS, and incubated in PBS + 40µM GlpQ or PBS + the equivalent volume of Buffer A for 15
104 min with rocking at 37°C. We then washed cells again 1X in PBS, and resuspended cells in PBS
105 supplemented with 200ug/mL of Concanavalin A-AlexaFluor 647 (Invitrogen, C21421) for 10min at 37°C,
106 with rocking. Concanavalin A is a lectin that binds glycosylation modifications along the teichoic acid
107 polymer[5,6]. We then washed cells again 1X in PBS, then resuspended samples in PBS for flow cytometry.
108 We performed our flow cytometry measurements with a Cytek Aurora set to 10,000 events per sample,
109 with gains adjusted to capture the full dynamic range of our population measurements. We consistently
110 calibrated the instrument to a low background (<10 events/second), and vigorously vortexed each sample
111 prior to acquisition. Since we were interested in statistics of the whole cell population, we performed
112 minimal gating (Fig. S6B). Since GlpQ preferentially cleaves non-glycosylated teichoic acids[2], the GlpQ-
113 mediated reduction in Concanavalin A staining for wild-type cells is likely an underestimate of GlpQ-

114 mediated teichoic acid cleavage. We used Δ*tagE* mutants to control for non-specific wheat-germ
115 agglutinin labeling, since TagE is responsible for teichoic acid glycosylation[7].

116 **Image Analysis and Tracking**

117 Cell tracking was performed using custom scripts written in FIJI (imagej.net), MATLAB (Mathworks, Natick,
118 MA, USA) and Python, all of which are available online at
119 *https://github.com/felixbarber/WTA_peptidoglycan_nanostructure*. We first applied the ImageJ scripts
120 image_process_updated.ijm and alignment_updated.ijm (for timelapse imaging, e.g. Fig. 1B) or
121 timepoint_imaging_v1.ijm (for discrete timepoint imaging, e.g. Fig. 1D) to generate the necessary tiff
122 image file structures for downstream segmentation and tracking in MATLAB. Our MATLAB timelapse
123 image analysis pipeline then involved the following steps: image alignment (imagealign_barber.m),
124 background removal (to avoid spurious detections, following eraseimagepart_barber.m), followed by cell
125 segmentation and tracking (BacTrack_barber.m). All cell segmentation was done based on phase contrast
126 images. Once phase contrast images were analyzed to generate individual cell masks (and cell tracks in
127 the case of timelapse imaging), we applied python scripts to analyze and plot the single cell characteristics,
128 and to integrate fluorescence data (for our discrete timepoint data series). The applicable python scripts
129 differ based on the purpose and plotting format for individual experiments, and a complete list of the
130 various different pipelines for different data formats is provided in the README file within our code
131 repository. Within these steps, we filtered our timelapse cell tracks to exclude cells tracks of 4 timepoints
132 or shorter, to exclude non-growing (dead) cells from analysis, and to remove sections of cell tracks with a
133 growth rate greater than two standard deviations away from the median growth rate (e.g. due to cell
134 divisions or mis-segmentations that combined multiple objects). For our cell staining experiments, we
135 calculated the cellular fluorescence by subtracting a background signal (obtained by normalizing a
136 Gaussian blur of the background signal across the cell mask), then calculating the statistics listed on the
137 pixel fluorescence values within individual cell masks. We performed spot detection (e.g. for Fig. 1D) with

138 SciKitImage's bloblog feature, using manually curated thresholds for each imaging condition, that were
139 then applied consistently across all images acquired using that condition (including across different cell
140 types).

141 **MreB filament tracking**

142 We detected and tracked our MreB and Mbl filaments using custom Python scripts as follows: first, we
143 generated our image file structures for downstream analysis using the ImageJ script tirf_processing.ijm.
144 We then applied the python script mreb_tracking_v3_py3.py, which detected, tracked and classified
145 filaments as follows: For filament detection, we applied SciKitImage's bloblog feature, using manually
146 curated thresholds to start each timelapse (that were then preserved within all timelapses acquired using
147 the same fluorescent fusion protein and imaging condition). These thresholds were iteratively reduced
148 throughout each step of a single time course to maintain roughly equivalent levels of spot detection. This
149 allowed us to correct for partial photobleaching of the fluorescent signal. We tracked individual puncta
150 across successive images (taken with a timestep of 2s) by calculating the minimum distance between all
151 annotated puncta, subject to a maximum displacement threshold of two pixels (equivalent to a linear
152 distance of 186nm based on our magnification and camera size, significantly greater than the average
153 displacement of a processive individual MreB or Mbl filament of roughly 80nm). We then filtered to
154 exclude all tracks with length 2 timepoints or less. To classify individual tracks as "ballistic", tracks had to
155 meet two criteria. First, we performed a linear regression on a log-log plot of distance (calculated between
156 successive points in each single puncta track and the track's starting position) versus time. If the slope of
157 this linear regression (the equivalent of ½ the "diffusion exponent" within single-molecule tracking, equal
158 here to 0.5 for diffusive behavior and 1.0 for ballistic, linear motion) was greater than 0.8, *and* if the R-
159 value of a linear regression for a standard plot of distances versus time (a metric for the goodness of fit
160 for linear motion) was greater than 0.9, we classified a track as ballistic.

161 **Cell lysis tracking**

162 We tracked cell lysis by perfusing cells with propidium iodide at a final concentration of 2µg/mL, imaging
163 every 5 min with 100 ms in the RFP channel at 10% power. Due to a high level of background signal
164 following cell lysis, we annotated cell lysis events using the semi-automated custom ImageJ macros
165 lysis_annotation_lysed_cells_updated.ijm and lysis_annotation_plain_cells_updated.ijm. These macros
166 allowed the user to provide annotations for lysed cells and all cells respectively within each image of a
167 propidium iodide-stained timecourse, which were then integrated and plotted using the python script
168 lysis_timelapses.py.

169 **Analysis of peptidoglycan composition**

170 Peptidoglycan was prepared from cell lysates and analysed by high-performance liquid chromatography
171 (HPLC) as previously described[8]: cell lysates were prepared from 500 mL of cell culture by boiling the cells
172 (100°C) for 30 min in the presence of 5% SDS to inactivate autolysins. The SDS was removed from the
173 insoluble cell wall preparation by repeated centrifugation (130,000 x *g* - 60 min)), the crude cell wall
174 washed with 1 M NaCl and twice with dionized water (dH_2O), and resuspension in dH_2O. The pellet was
175 resuspended in 2 to 4 mL of dH_2O, 1/3 volume of acid-washed glass beads (diameter of 0.17–0.18 mm,
176 Sigma, München, Germany) was added, and cell walls were disrupted in a FastPrep machine (FP120,
177 Thermo Scientific, Hemel Hempstead, UK). Broken cell walls were separated from the glass beads through
178 filtration and collected by ultracentrifugation as above. Cell walls were incubated at 4°C with DNase A and
179 RNase (for 2 h) and then with trypsin (18 h), and then incubated with 1% SDS at 80°C for 15 min. The cell
180 walls were then washed with 8 M LiCl, 20 mM EDTA and water, and lyophilized. The attached wall teichoic
181 acid was removed by treatment with 48% hydrofluoric acid (48 h at 4°C). The resulting peptidoglycan was
182 recovered by centrifugation and washed once with 50 mM Tris/HCL pH 7.0 and then with ice-cold distilled
183 water until a neutral pH was achieved. The peptidoglycan was digested with cellosyl (gift from Hoechst,

184 Germany) and the resulting muropeptides recovered were reduced with sodium borohydride and
185 separated by HPLC on a 250 × 4.6 mm 3-µm Prontosil 120-3-C_{18} AQ reversed-phase column (Bischoff,
186 Leonberg, Germany) maintained at 52°C. A 270 min linear gradient reverse phase separation was
187 performed using 40 mM $NaPO_4$ pH 4.5, 0.003%NaN_3 (buffer 1, called buffer A in prior work but renamed
188 here to avoid confusion with our GlpQ protein buffer) and 40 mM $NaPO_4$ pH 4.0, 20% MeOH (buffer B)[9].
189 Muropeptides were detected by their absorbance at 202 nm and structures were assigned by comparison
190 to published chromatograms[9].

191 **Permeability Assays**

192 Cells were grown to log-phase and diluted 20-fold into a pre-warmed medium within the loading well of
193 a pre-heated CellASIC B04A microfluidic flow cell. The cells incubated for an additional 30 minutes prior
194 to loading into the imaging chamber. While imaging, fresh medium was perfused through the flow cell.
195 The cell-trapping mechanism used by the microfluidic chips had no detrimental effect on the elongation
196 or morphology of cell chains, as compared with cells growing on agarose pads or liquid culture[7].

197

198 To perform membrane lysis, we exchanged the medium in the flow cell with media + 5% N-
199 lauroylsarcosine (Sigma Aldrich L9150) for two minutes. We monitored detergent exchange using the dye
200 AlexaFluor 647 at a final media concentration of 5 µg/mL and imaged with CY5 illumination, 640 nm
201 excitation at 10% intensity and 50 ms exposure. After membrane lysis, the detergent in the flow cell was
202 exchanged for media to wash the cells.

203

204 Because both tunicamycin and GlpQ are temperature sensitive, all handling steps were performed to
205 better preserve reagent stability: tunicamycin and GlpQ were introduced into the microfluidic device

206 concurrently with the cells. At the end of the culture back-dilution, a 5 mg/mL tunicamycin stock aliquot
207 was thawed briefly and subjected to two successive 1:100 dilutions in LB before being loaded into the
208 chip. GlpQ aliquots were thawed on ice for approximately 30 min and diluted in PBS immediately prior to
209 use. Since PBS-mediated hydrolysis is sensitive to divalent cation concentration, an equal volume of Buffer
210 A was diluted in PBS as a control.

211

212 For the experiments in Figure 3A, cells expressing mNeonGreen were imaged every minute in our GFP
213 channel (480 nm excitation from an LED light source, Lumencor Aura Light Engine) at 100% power and 50
214 ms exposure. To mitigate photobleaching, no images were acquired were acquired from one minute after
215 the onset of tunicamycin treatment to five minutes prior to detergent exchange. Wild-type and Δ*ponA*
216 cells were exposed to 0.5 µg/mL tunicamycin for 10 minutes and 20 minutes respectively, corresponding
217 to time points during which Rod complex activity halts in each strain.

218

219 For the experiments in Figure 3B, cells expressing mNeonGreen were imaged in our GFP channel at 100%
220 power and 50 ms exposure: every minute for seven minutes, not acquired for eight minutes during Buffer
221 A/GlpQ perfusion, every minute for 10 minutes, and then every five minutes for 1 hour. Cells were
222 exposed to GlpQ or Buffer A for 15 minutes prior to membrane lysis.

223

224 For the experiment in Figure 3C, cells expressing a tetracysteine-tagged ubiquitin, we imaged in our GFP
225 channel at 10% power and 50 ms exposure every minute for the first 10 minutes and every five minutes
226 afterwards. To label the tetracysteine-tagged ubiquitin, we incubated cells with 1 µM FlAsH-EDT_2 (4',5'-
227 bis(1,3,2-dithiarsolan-2-yl)-3',6'-dihydroxy-spiro[isobenzofuran-1(3H),9'-[9H]xanthen]-3-one; Cayman

228 Chemical 20704) for one hour prior to diluting the cells into the loading well, which also had 1 µM FlAsH-
229 EDT_2 in the medium. To perform membrane lysis and wall teichoic acid hydrolysis simultaneously, the
230 medium in the flow cell was exchanged with PBS + 5% N-lauroylsarcosine + GlpQ (or Buffer A) for two
231 minutes. We then perfused the cells with PBS + GlpQ (or Buffer A). As a control for non-specific binding of
232 FlAsH, we performed the same experiment in Buffer A with uninduced cells and subtracted the mean
233 uninduced fluorescence from the fluorescence trace of each cell.

234

235 The fluorescence from the frames during lysis were interpolated. The cellular trace was corrected for
236 photobleaching and then normalized to the final pre-lysis frame.

237 To perform the photobleaching controls[3], cells were imaged at one frame per minute during the initial
238 seven minutes of the experiment prior to cell lysis. After membrane lysis, the cells were imaged at frame
239 rates that were much more rapid than the rate of protein efflux.

240

241 **Limitations:** our permeability assay can quantitatively assess pores in the cell wall empirically, but cannot
242 resolve the distribution of pore sizes[3]. For example, we could not distinguish between 10 pores that allow
243 the passage of one mNeonGreen enzyme at a time, or one pore that allows 10 mNeonGreen enzymes to
244 pass through simultaneously. Additionally, while we controlled for the effect of the isoelectric point (pI)
245 of the probe, we have not yet explored whether there are other electrical properties of the probe that
246 influence permeability through the wall (for example, the net charge or distribution of acidic/basic
247 residues throughout the protein).

248

249 **Permeability photobleaching correction**

Population-averaged fluorescence traces were fit to a single exponential:

$$y = A\, e^{-x\rho}$$

where y = normalized fluorescence, A is the initial post-lysis normalized fluorescence value, ρ = the photobleaching constant, and x is the frame number (Figure S7, S9).

For mNeonGreen, the mean background value is subtracted from the mean fluorescence of each cell and normalized by the fluorescence of the final pre-lysis frame.

For FlAsH, the mean background value and mean autofluorescence is subtracted from the mean fluorescence of each cell. The mean autofluorescence was obtained by measuring the fluorescence of uninduced cells incubated with FlAsH-EDT_2.

To correct for photobleaching, the expected loss of fluorescence due to photobleaching was calculated,

$$dC_B = C_i * \rho$$

where C_B = bleached fluorophore, C_i = measured fluorescence in the *i*th frame, and r = photobleaching constant (obtained from the photobleaching control). The total loss of fluorescence (dC_T) in each frame is adjusted to account for the expected loss of fluorescence due to photobleaching,

$$dC_T = C_{i+1} - C_i$$

$$dC_U = dC_T + dC_B$$

$$C_{i+1} = C_i + dC_U$$

270 where dC_U is the change in unbleached fluorophore.

271

272 **Transmission Electron Microscopy**

273 We performed transmission electron microscopy on thin sections of formaldehyde-fixed freeze-
274 substituted *B. subtilis* cells as follows: we grew cultures of wild-type and Δ*ponA* cells to log-phase, then
275 back diluted into either fresh LB medium or LB supplemented with 0.5μg/mL tunicamycin for 30 min. We
276 then pelleted cells by centrifugation for 4 min at 3500 RPM, washed 1X in PBS, and resuspended in 1 mL
277 freshly made LRR fixative solution[10] (0.5 mL 0.15% ruthenium red, 125 µL 16% formaldehyde, 0.0155
278 g lysine acetate (Sigma); distilled water to 1 mL).

279

280 Samples were then subjected to high pressure freezing and freeze substitution. 3 mm planchettes
281 100 mm deep were lightly coated with hexadecene before being filled with approximately 1.2mL of fixed
282 sample. An absorbent filter paper was used to soak out extra liquid, and then the sample was allowed to
283 dry slightly for ~ 5 min. The hats were then sealed in the planchette holder for high-pressure freezing
284 (Leica ICE High Pressure Freezing Platform, Leica Microsystems). The frozen samples were immediately
285 transferred into liquid nitrogen and then into cryovials containing freeze substitution solutions (2 mL
286 cryovials (Nalgene) containing 2% (wt/vol) osmium tetroxide (OsO_4) and 0.1% (wt/vol) uranyl acetate in
287 anhydrous acetone with 0.075% (wt/vol) ruthenium red and 2% H_2O) at liquid nitrogen temperature. The
288 samples were brought into a Leica AFS2 EM freeze substitution unit (Leica Microsystems) and left in the -
289 90°C for 79 hours. Since the acetone:osmium mixture liquifies at -90ºC, the hats were slowly submerged
290 in the freeze substitution media. The temperature of the unit was raised 5°C per hour to –60°C and
291 incubated for 12 hours, then to –30°C for an additional 6 hours, and finally to a temperature of 0°C for 6
292 hrs.

293

294 After removal from freeze substitution unit, samples were washed in pure ethanol 3 x 1 hour on ice to
295 rinse out osmium. They were then washed with 1:1 100% ethanol:LR White resin for 2 hours on ice, 1:2
296 100% ethanol:LR White resin overnight at 4ºC, pure LR White resin for 8 hours on ice, and finally pure LR
297 White resin overnight at 4ºC. Samples were then embedded in gelatin capsules filled with LR White resin
298 at room temperature and polymerized for 48 hours at 55-60 ºC. Thin sections were cut onto 200 mesh
299 grids and counterstained with 4% aqueous uranyl acetate for 5 min. Stained grids were examined using a
300 JEOL1400 Flash transmission electron microscope (Japan) and photographed with a Gatan Rio 16 camera
301 (Gatan Inc. Pleasanton, CA). All chemicals and EM grids are purchased from Electron Microscopy Sciences,
302 Hatfield, PA.

303 Note: TEM sample preparations of wild-type and Δ*ponA* mutants were performed as separate batches,
304 with Δ*ponA* mutant samples being exposed to LRR fixative solution for up to 10 min longer than wild-
305 type cells immediately following lysis. We attribute this difference to the darker cell wall appearance
306 of Δ*ponA* mutants relative to wild-type cells, making it difficult to compare absolute cell wall
307 thickness between these cell types.

308 **Data Availability**

309 All datasets presented herein will be made publicly available.

310 **Code Availability**

311 All code used herein is publicly available at:
312 https://github.com/felixbarber/WTA_peptidoglycan_nanostructure

313

314 **Methods References**

315 1. Flórez, A. F. *et al.* BatCRISPRi: Bacillus titratable CRISPRi for dynamic control in Bacillus subtilis.
316 2023.11.01.565046 Preprint at https://doi.org/10.1101/2023.11.01.565046 (2023).
317 2. Myers, C. L. *et al.* Identification of Two Phosphate Starvation-induced Wall Teichoic Acid Hydrolases
318 Provides First Insights into the Degradative Pathway of a Key Bacterial Cell Wall Component*. *Journal*
319 *of Biological Chemistry* **291**, 26066–26082 (2016).
320 3. Akbary, Z. *et al.* Peptidoglycan turnover promotes active transport of protein through the bacterial
321 cell wall. 2025.09.12.675941 Preprint at https://doi.org/10.1101/2025.09.12.675941 (2025).
322 4. Phosphate-buffered saline (PBS). *Cold Spring Harb Protoc* **2006**, pdb.rec8247 (2006).
323 5. Koyano, Y., Okajima, K., Mihara, M. & Yamamoto, H. Visualization of Wall Teichoic Acid Decoration in
324 Bacillus subtilis. *Journal of Bacteriology* **0**, e00066-23 (2023).
325 6. Lang, W. K. & Archibald, A. R. Relation between wall teichoic acid content and Concanavalin A binding
326 in Bacillus subtilis 168. *FEMS Microbiology Letters* **20**, 163–166 (1983).
327 7. Allison, S. E., D'Elia, M. A., Arar, S., Monteiro, M. A. & Brown, E. D. Studies of the genetics, function,
328 and kinetic mechanism of TagE, the wall teichoic acid glycosyltransferase in Bacillus subtilis 168. *J Biol*
329 *Chem* **286**, 23708–23716 (2011).
330 8. Bui, N. K. *et al.* Isolation and analysis of cell wall components from *Streptococcus pneumoniae*.
331 *Analytical Biochemistry* **421**, 657–666 (2012).
332 9. Atrih, A., Bacher, G., Allmaier, G., Williamson, M. P. & Foster, S. J. Analysis of peptidoglycan structure
333 from vegetative cells of Bacillus subtilis 168 and role of PBP 5 in peptidoglycan maturation. *J Bacteriol*
334 **181**, 3956–3966 (1999).
335 10. Hammerschmidt, S. *et al.* Illustration of Pneumococcal Polysaccharide Capsule during Adherence
336 and Invasion of Epithelial Cells. *Infection and Immunity* **73**, 4653–4667 (2005).

337 11. Koo, B.-M. *et al.* Construction and Analysis of Two Genome-scale Deletion Libraries for Bacillus
338 subtilis. *Cell Syst* **4**, 291-305.e7 (2017).
339 12. Liechti, G. W. *et al.* A new metabolic cell-wall labelling method reveals peptidoglycan in
340 Chlamydia trachomatis. *Nature* **506**, 507–510 (2014).
341

342 **Acknowledgements**

343 ERR and FB were supported by NSF-CAREER grant 2047404. WV received funding from the UK
344 Biotechnology and Biological Sciences Research Council (BBSRC) (BB/W013630/1). ZA was supported by
345 NIH grant R35GM143057**.** We thank Ethan Garner and the Garner Lab (both past and present) for
346 generously sharing strains; we have particularly benefitted from strains built by prior Garner Lab members
347 Mrinal Kapoor, Mike Dion, Yingjie Sun and Sean Wilson. We also thank the Brown lab for sharing their
348 GlpQ expression construct. We thank Dr. Daniela Vollmer for preparation of peptidoglycan. We thank
349 NYULH Microscopy Lab Alice Liang, Jason Yin and Jason Liang (partially supported by NYU Cancer
350 Center Support Grant NIH/NCI P30CA016087) for consultation and timely preparation of the
351 electron microscopy works.

352 **Author Contributions**

353 FB, ZA, ZY, JB and LPL performed the experiments. FB, ZA, ZY, JB and LPL analyzed the data. FB and ER
354 wrote the manuscript.

355 **Declaration of Interests**

356 The authors declare no competing interests.

357

358 **Extended Data: Tables**

359 **Table S1:** List of strains used in this study.

Strain ID	Genotype/Plasmid	Figures in this study	Source	Method
bGL01	WT	1(B,D,E), 2(A-C), S1(A-C), S2(A,B,E-H), S4(B), S5, S6(A,E-G), S7, S8(C), S10(A), S11(A,C), S12	Gift from Garner Lab	NA
bEG176	*ΔtagO::erm*	1E, S1(B,C), S5, S7(A)	Gift from Garner Lab	NA
bEG291	*ΔtagO::erm, ycgO::PxylA-tagO cat*	S2(C,D), S4(A), S6(B), S12(B)	Gift from Garner Lab	NA
bYS009	*ΔmreB::mreB-40aa-mNeonGreen*	S3(D-F)	Gift from Garner Lab	NA
bYS147	*amyE::Phyperspank-mNeonGreen::erm*	3(A,B)	Gift from Garner Lab	NA
bMD122	*Δmbl::sfGFP-mbl spec*	1(C,E), 3(E), S3(A-C,G-I), S9, Videos S2-S7,S12-S15	Gift from Garner Lab	NA
bMD599	*ΔponA::kan*	1(D), 2(A-C), 3(D,F), S2(E,F), S6(A), S8(C), S10(B,C), S11(B,D)	Gift from Garner Lab	NA
bMD643	*ΔponA::ponA-FLAG spec*	2(E), S6(G)	Gift from Garner Lab	NA
bMK210	*amyE::erm-Phyperspank(MkII)-mNeonGreen-15aa-ponA*	2(D), S6(C,D), Videos S8-9	Gift from Garner Lab	NA
bMK296	*amyE::erm-Pxyl-ponA(E115A), ΔponA::cat*	2(C), S6(A)	Gift from Garner Lab	NA

bSW23	*ΔcwlO::erm*	S11(A,C) , S12(A)	Gift from Garner Lab	NA
bSW295	*ΔlytE::kan*	S11(A,C), S12(A)	Gift from Garner Lab	NA
bFB012	*Δmbl::sfGFP-mbl spec, ΔtagO::erm, ΔycgO::PxylA-tagO*	S3(J-L)	This study	bEG291 transformed with bMD122 gDNA.
bFB22	*ΔlytE::kan, Δmbl::sfGFP-mbl spec*	S11(H-J)	This study	bSW295 transformed with bMD122 gDNA.
bFB26	*ΔcwlO::erm*, *Δmbl::*sfGFP-mbl spec	S11(E-G)	This study	bSW23 transformed with bMD122 gDNA.
bFB83	*ΔponA::kan, Δmbl::sfGFP-mbl spec*	2(F), Videos S10,S11	This study	bMD599 transformed with bMD122 gDNA.
bFB87	*ΔponA::kan, ΔcwlO::erm*	S11(B,D)	This study	bSW23 transformed with bMD599 gDNA.
bFB93	*ΔponA::erm, ΔlytE::kan*	S11(B,D)	This study	bSW295 transformed with ponA::erm construct from BKE22320 (Bacillus genetic stock center[11]).
bFB145	*ΔponA::ponA(S390A) kan*	1(D), 2(A,C), S6(A)	This study	bGL01 transformed with Gibson assembly of oFB166/155 fusion PCR product (from oFB166/oFB157 and oFB156/oFB155 PCR products with bGL01 gDNA) and oFB154/oFB148 PCR product with bMD599 gDNA.
bFB149	*ΔponA::ponA kan*	Video S1	This study	Same as bFB145 but did not take up point mutation in S390A.
bFB155	*ΔtagE::erm*	S7(A)	This study	bGL01 transformed with PCR product of oTY001 and oTY002 on BKE35730 gDNA.
bFB177	*ΔtagO::erm, ycgO::PxylA-tagO cat ΔlytE::kan*	S12(B)	This study	bEG291 transformed with bSW295 gDNA.
bFB215	*ΔtagO::erm, ΔycgO::PxylA-tagO cat ΔponA::kan*	S6(B)	This study	bEG291 transformed with bMD599 gDNA.
bFB221	*ΔcwlO::kan*	NA	This study	bGL01 transformed with PCR product of oFB049 and oFB050 on BKK34800 gDNA.
bFB226	*ΔpbpD::kan*	NA		bGL01 transformed with PCR product of oTY038 and oTY039 on BKK31490 gDNA.

bFB236	*ΔtagO::erm, ycgO::PxylA-tagO cat, ΔcwlO::kan*	S12(B)	This study	bEG291 transformed with bFB221 gDNA.
bFB262	*ΔtagO::erm, ΔycgO::PxylA-tagO cat, ΔpbpD::kan*	S6(B)	This study	bEG291 transformed with bFB226 gDNA.
bFB264	*ΔtagO::erm, ΔycgO::PxylA-tagO cat, ΔponA::ponA(S390A)-kan*	S6(B)	This study	bEG291 transformed with bFB145 gDNA.
bFB305	*ΔtagO::erm, ycgO::PxylA-tagO, ΔlytF::kan*	S12(B)	This study	bEG291 transformed with PCR product of oFB270 and oFB271 on BKK09370 gDNA.
bFB317	*ΔponA::ponA-FLAG spec ΔsigI::kan*	S6(I)	This study	bMD643 transformed with PCR product of oFB279 and oFB281 on BKK13450 gDNA.
bFB319	*ΔponA::ponA(ΔIDR)-FLAG-kan*	2(C), S6(A)	This study	bGL01 transformed with Gibson assembly of PCR product of oFB159 and oFB290 on bGL01 gDNA and PCR product of oFB289 and oFB148 on bFB145 gDNA.
bER461	*Escherichia coli BL21(DE3) pDest17-glpQ*	3(B,C,D,E,F), S7, S8, S9, S10, S11	Gift from Brown Lab[2]	NA
bER565	*amyE::Phyperspank-ubiquitin-TC::erm*	NA	Rojas Lab	See Akbary *et al*.[3]
bER607	*ΔponA::kan, amyE::Phyperspank-ubiquitin-TC::erm*	3(C), S8(A,B)	Rojas Lab	bMD599 transformed with bER565 gDNA.
bER608	*ΔponA::kan, amyE::Phyperspank-mNeonGreen::erm*	3(A,B)	Rojas Lab	bMD599 transformed with bYS147 gDNA.
BKE35730	*trpC2 ΔtagE::erm*	NA	BGSC	
BKK31490	*trpC2 ΔpbpD::kan*	NA	BGSC	
BKE22320	*trpC2 ΔponA::erm*	NA	BGSC	
BKK09370	*trpC2 ΔlytF::kan*	NA	BGSC	
BKK34800	*trpC2 ΔcwlO::kan*	NA	BGSC	
BKK13450	*trpC2 ΔsigI::kan*	NA	BGSC	

360

361 **Table S2:** List of primers used in this study.

Name	Sequence	Purpose
oFB008	CAGGGAGCACTGGTC	Confirm insertion of bMD122 mbl construct in bFB26.
oFB020	CTTCGTATAATGTATGCTATACGA	Confirm insertion of ponA::erm in bFB93.
oFB041	ATTTTTATTCAATTAGGGAATATCTTGTTC CATCCGATTATCACGCAGGGAGCACTGGTC	Confirm insertion of bMD122 mbl construct in bFB26.
oFB049	CTTATGAAGTGCTTTCTCATAATG	Confirm deletion of cwlO in bFB221, bFB236.
oFB050	ATGTGAAACTCGTATGACAG	Confirm deletion of cwlO in bFB221, bFB236.
oFB051	TGCTTGTTTAGTTGTCACAT	Confirm deletion of lytE in bFB177.
oFB052	TCAAAGCTGTGATTCAGTG	Confirm deletion of lytE in bFB177.
oFB053	CTATACGAATAGCTTAGACAGC	Confirm construction of bFB145, bFB149, bFB177, bFB215.
oFB054	TAACAAGACGAACTCCAATTC	Confirm construction of bFB145, bFB149, bFB177, bFB215.
oFB055	GCGAACAATCAAGATAGGG	Confirm insertion of bMD122 mbl construct in bFB12, bFB22, bFB83.
oFB056	TCGATCAATGCAATGTCTG	Confirm insertion of bMD122 mbl construct in bFB12, bFB22, bFB83.
oFB059	CACGAAAAACAAATGATTAAGAAGCGTGCA AAAATCACGAATTAATTCTGCTCCCTCGCT	Confirm insertion of bMD122 mbl construct in bFB26.
oFB063	TTCTGCTCCCTCGCT	Confirm insertion of bMD122 mbl construct in bFB26.
oFB077	GTGAATAGCTCACTTATCAGATTA	Confirm insertion of ponA::erm in bFB93.
oFB094	TACAGCTCGATAATCTTTTCAG	Confirm construction of bFB221, bFB236, bFB262, bFB305.
oFB095	TTTGAACGGCATGATGG	Confirm construction of bFB221, bFB236, bFB262, bFB305.
oFB115	GAAAGGTTGATTAACGAAAGG	Confirm insertion of ponA deletion construct from bMD599 into bFB87.
oFB116	CGATAAAACCTCCTGTTAAAAC	Confirm insertion of ponA deletion construct from bMD599 into bFB87. Confirm construction of bFB264.
oFB146	CAATTGAGACAGCTGCTT	Amplify ponA::erm to construct bFB93.
oFB147	GAGGAGAACAATTCTGGC	Confirm insertion of ponA::erm in bFB93.
oFB148	AGGTGACAATCGTGTTAAAT	Amplify ponA::erm to construct bFB93. Construction of bFB145, bFB149, bFB319. Confirm construction of bFB215.
oFB149	CTCAGTTTCCGCTACATTG	Confirm construction of bFB93, bFB145, bFB149, bFB319.
oFB154	AAATTAAACAAAAAAGCCGTCACCTTTGG	Construction of bFB145, bFB149.

	GGTGATGGCTTTTTTGTTCTGCTCCCTCGCT	
oFB155	ATCACCCCAAAGGTGACGGCTTTTTTGTTTA ATTTGTTTTTTCAATGGATGATGAGTTTG	Construction of bFB145, bFB149.
oFB156	CTCAAACTAAGGCACAGCCTGGTGCGACCA TAAAACCGATTTTGGACTACGGACCAGTTA	Construction of bFB145, bFB149.
oFB157	CCAAAATCGGTTTTATGGTCGCACCAGGCTG TGCCTTAGTTTGAGTAGCATAGTTAAAGC	Construction of bFB145, bFB149.
oFB159	TGGACTACGGACCAGTTA	Confirm construction of bFB145, bFB149. Construction of bFB319.
oFB164	CTCAGAAGCTTTCTGATGG	Confirm construction of bFB215.
oFB166	GATGCGGTATACCTTCTCAA	Construction of bFB145, bFB149.
oFB168	CGCAATTACTCTAAAGATGAAATT	Confirm construction of bFB319.
oFB171	CACACCGCAATATACAGC	Confirm construction of bFB319.
oFB173	AAGACTCAGGATGATACACA	Confirm construction of bFB264.
oFB174	CGGTATAATCTTACCTATCACC	Confirm construction of bFB319.
oFB245	CGTATGGCAATGGGTCTTG	Confirm construction of bFB262.
oFB246	GTTCATATTTATCAAGCTTTATAATAGCATAA TGGCTA	Confirm construction of bFB262.
oFB269	CTTGTCTCAAGTTGTCGGTATG	Confirm construction of bFB305.
oFB270	TCTGCTCTTTACAGCTGA	Construction of bFB305.
oFB271	CTGTTGAAAGTACAGGAGC	Construction of bFB305.
oFB272	CACACGGATTTGATTGATCTAAGC	Confirm construction of bFB305.
oFB279	GCATATTATTGACGTATAAAATCATATTTCTTG	Construction of bFB317.
oFB281	TGAACCTTGGTTCTGATACA	Construction of bFB317.
oFB289	ATGAGGTGCCAAAAGCTGATTATAAAGATGA TGATGATAAATAAACAAAAAAGCCGTCAC	Construction of bFB319.
oFB290	GACGGCTTTTTTGTTTATTTATCATCATCATCT TTATAATCAGCTTTTGGCACCTCATAA	Construction of bFB319.
oTY001	CACCGTACAGAAATATGCG	Construction of bFB155.
oTY002	ATATATTCGTAAATCGCTCTCG	Construction of bFB155.
oTY003	CGGAATCCATAATGGAAGC	Confirm construction of bFB155.
oTY004	AACATAACCGTCTGAATAACC	Confirm construction of bFB155.
oTY038	GATTCATCCCGACATCTCT	Construction of bFB226.
oTY039	GTAAGCTAGCCATTTCAGC	Construction of bFB226.

362

363 **Extended Data: Figures**

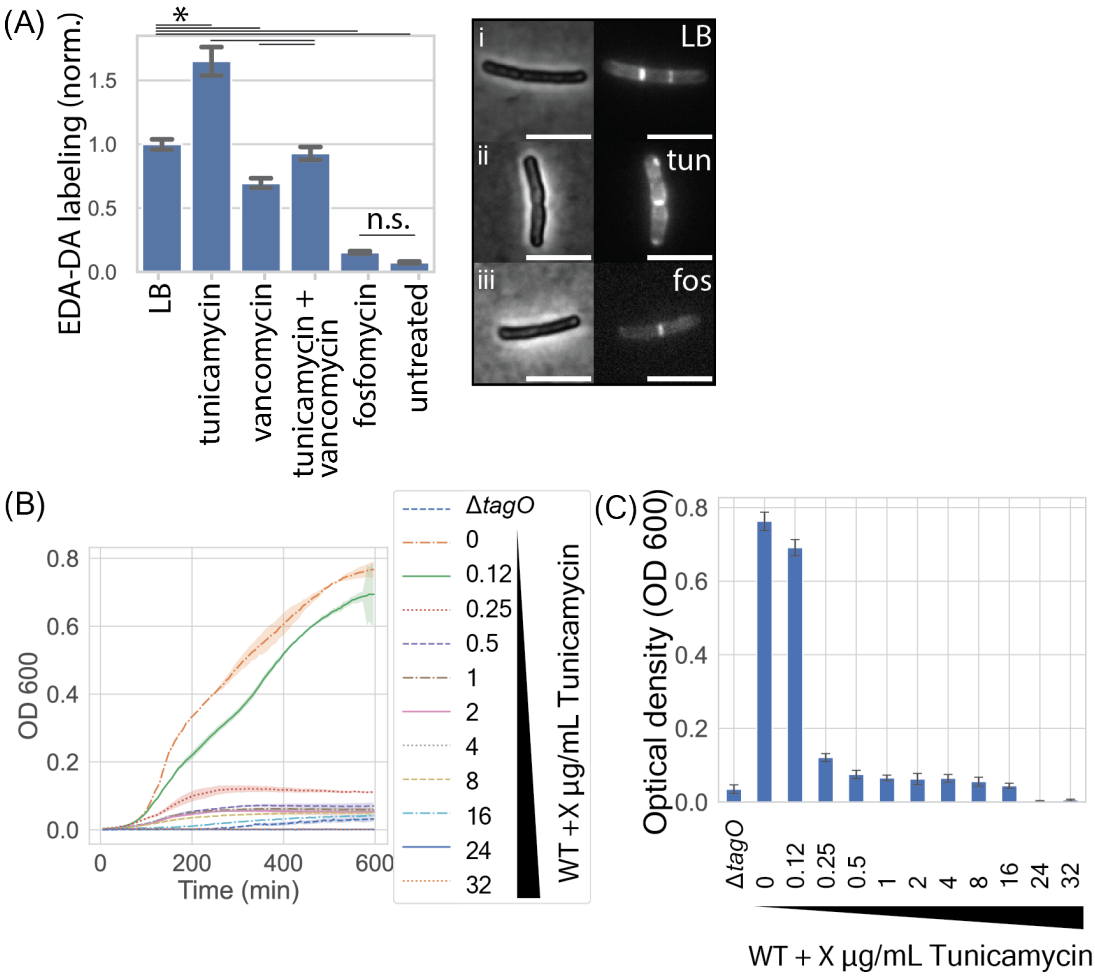

364

365 **Figure S1: (A) Low doses of tunicamycin do not decrease peptidoglycan precursor synthesis.** We
366 pulsed exponentially growing cells with the dipeptide D-amino acid EDA-DA (ethynyl-D-alanine D-
367 alanine), which is incorporated into peptidoglycan precursors cytosolically[12], before fixing and
368 "clicking" with AlexaFluor 488 azide (*Methods*). Plot shows average intensity of AF488 labeling for
369 cells co-treated with the drugs shown, normalized against staining for cells grown in LB
370 supplemented with EDA-DA alone. Staining increased during tunicamycin treatment (relative to
371 EDA-DA alone), and during co-treatment with both tunicamycin and vancomycin (relative to co-
372 treatment with vancomycin), consistent with a rerouting of precursors to peptidoglycan synthesis
373 during TagO inhibition. Staining decreased only partially for vancomycin treatment relative to LB
374 alone, consistent with AF488 labeling both nascent peptidoglycan and lipid II. Fosfomycin treatment
375 arrests peptidoglycan precursor synthesis at the inner face of the plasma membrane so is a negative
376 control. Untreated cells were not exposed to EDA-DA but were clicked with AF488 azide to control

377 for off-target AF488 labeling. Analysis was performed over 1,533 cells (LB, 5 experimental
378 replicates), 1,063 cells (tunicamycin, 5 experimental replicates), 810 cells (tunicamycin +
379 vancomycin, 3 experimental replicates), 1,081 cells (vancomycin, 4 experimental replicates), 555
380 cells (fosfomycin control, 4 experimental replicates), and 473 cells (untreated, 4 experimental
381 replicates). All differences between conditions were significant (one-way ANOVA followed by
382 Tukey's honestly significant difference (HSD) post-hoc test, $P<0.01$), with the exception of
383 comparisons between fosfomycin-untreated and between LB-tunicamycin+vancomycin. Inset:
384 phase contrast and fluorescence micrographs of cells from (i) LB, (ii) tunicamycin and (iii) fosfomycin
385 conditions. Fluorescence micrographs are identically saturated. Scale bars 5μm. **(B-C) Low**
386 **tunicamycin concentrations inhibit growth to precisely the same extent as deletion of *tagO.* (B)** Growth
387 curves of cells grown with increasing tunicamycin concentrations in bulk culture. **(C)** Saturating culture
388 density plotted for data from (A). Representative data from one of three biological replicates, with 4
389 technical replicates per condition. Error bars show 95% confidence intervals based on bootstrap
390 analysis. Complete growth arrest consistently occurs at either 16μg/mL or 24μg/mL tunicamycin.

391

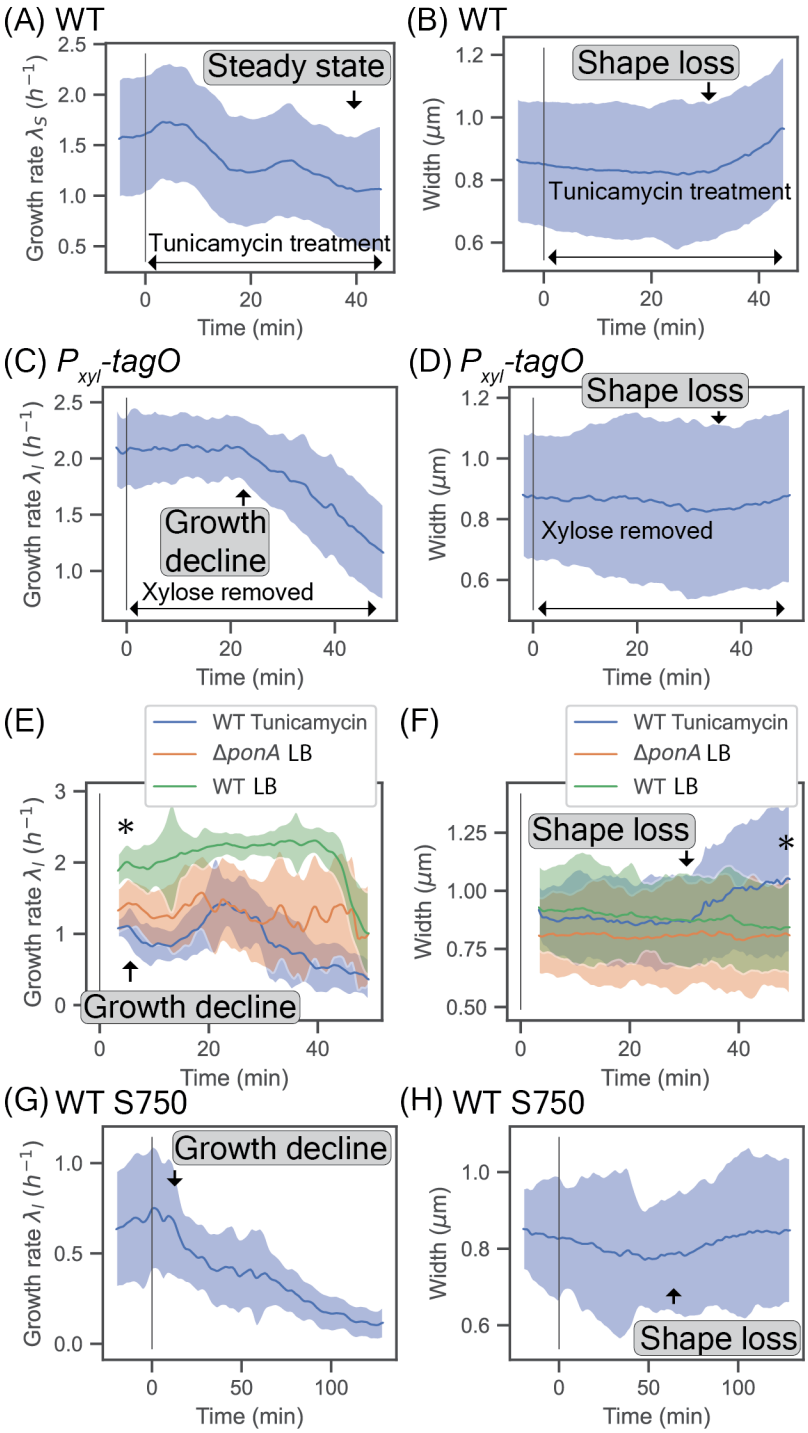

392

393 **Figure S2: (A)** Cell surface area growth rate $\lambda_S = \frac{1}{S}\frac{dS}{dt}$ for wild-type cells during 0.5μg/mL tunicamycin

394 treatment. Analysis performed over 1,927 discrete cell tracks from 3 biological replicates. In all plots,

395 solid lines show smoothed population medians, error bars show standard deviations across cells. Black

396 lines show onset of perturbation (tunicamycin treatment, inducer depletion or cell spotting onto agarose
397 pads). **(B)** Cell width of wild-type cells during 0.5µg/mL tunicamycin timecourse. Solid line shows
398 smoothed population median, error bars show standard deviation. Black lines show onset of tunicamycin
399 treatment. Increase in width corresponds to gradual loss of cell shape. Analysis performed over 3,737
400 discrete cell tracks from 3 biological replicates. **(C-D)** Cell properties during growth response of P_{xylA}-*tagO*
401 cells to xylose depletion. **(C)** Cell length growth rate. Analysis performed over 1,217 discrete cell tracks
402 from 3 biological replicates. **(D)** Cell width. Analysis performed over 1,846 discrete cell tracks from 3
403 biological replicates. **(E-F)** Cell growth and shape response to tunicamycin treatment on agarose pads. **(E)**
404 Cell length growth rate. Analysis performed over 204 discrete cell tracks from 4 biological replicates (WT
405 LB), 160 discrete cell tracks from 3 biological replicates (WT tunicamycin) and 93 discrete cell tracks from
406 3 biological replicates (Δ*ponA* LB). Growth rate during tunicamycin-treatment shows immediately slower
407 growth, with oscillations, followed by a sustained secondary decline at approximately 30 min (coincident
408 with shape loss, see (F)). WT cells grown in LB alone showed an abrupt growth decline at 45 min with no
409 shape loss. This late-stage decline was not observed for the slower-growing Δ*ponA* cells, consistent with
410 local nutrient depletion in these roughly 1mm-thin agarose pads. WT LB and WT Tunicamycin time
411 courses show statistical significance based on Student's T-test, $P<0.01$, calculated at first
412 measured timepoint. **(F)** Cell width. Analysis performed over 535 discrete cell tracks from 4 biological
413 replicates (WT LB), 432 discrete cell tracks from 3 biological replicates (WT tunicamycin) and 214 discrete
414 cell tracks from 3 biological replicates (Δ*ponA* LB). WT LB and WT Tunicamycin time courses show
415 statistical significance based on Student's T-test, $P<0.01$, calculated at last measured timepoint (63
416 min). **(G-H)** Time course of 0.5µg/mL tunicamycin exposure for WT cells grown in S750 media. **(G)** Cell
417 length growth rate. Analysis performed over 249 discrete cell tracks from 2 biological replicates. **(H)** Cell
418 width. Analysis performed over 307 discrete cell tracks from 2 biological replicates.

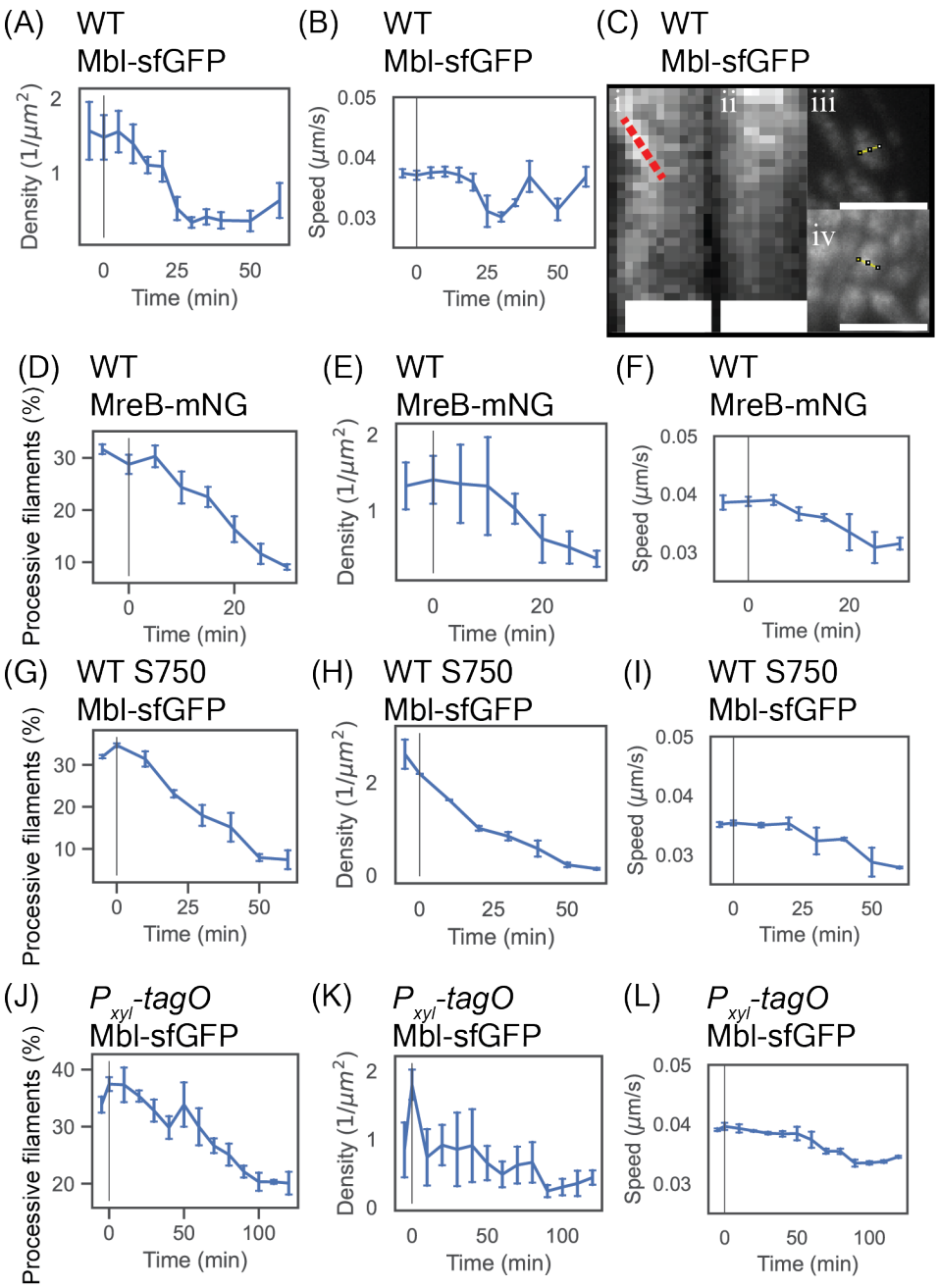

Figure S3: (A-B) Mbl-sfGFP activity time course for wild-type cells during 0.5µg/mL tunicamycin treatment. Analysis performed on 62,901 discrete filament tracks from 4 biological replicates. All error bars show 95% confidence intervals across biological replicates based on bootstrap analysis. **(A)** Spatial density of processive filaments. **(B)** Average speed of processive filaments. **(C)** (i-ii) Representative kymographs from TIRF imaging of Mbl-sfGFP cells after 60 min tunicamycin treatment. Red dotted line follows a processive Mbl filament. Scale bars 1μm. (iii-iv) TIRF micrographs showing whole cells during a single timepoint of the kymographs in (i-ii) respectively. Yellow lines show kymograph traces. Scale bars 5µm. **(D-F)** MreB-

427 mNeonGreen activity time course for wild-type cells during 0.5µg/mL tunicamycin treatment. Analysis
428 performed on 30,805 discrete filament tracks from 3 biological replicates. **(D)** Percentage of processive
429 filaments. **(E)** Spatial density of processive filaments. **(F)** Average speed of processive filaments. **(G-I)** Mbl-
430 sfGFP activity time course for wild-type cells grown in S750 media during 0.5µg/mL tunicamycin
431 treatment. Analysis performed on 9,859 discrete filament tracks from 2 biological replicates. **(G)**
432 Percentage of processive filaments. **(H)** Spatial density of processive filaments. **(I)** Average speed of
433 processive filaments. **(J-L)** Mbl-sfGFP activity time course of of P_{xylA}-*tagO* cells during xylose depletion.
434 Analysis performed on 55,542 discrete filament tracks from 3 biological replicates. **(J)** Percentage of
435 processive filaments. **(K)** Spatial density of processive filaments. **(L)** Average speed of processive filaments.

436

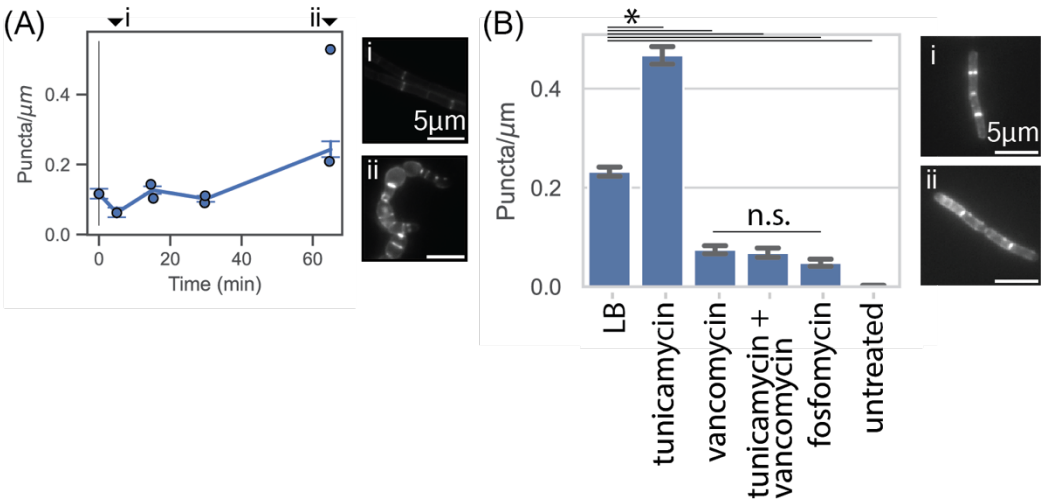

Figure S4. (A) Mean fluorescent puncta per cell (normalized to cell length) for P_{xylA}-*TagO* cells during xylose depletion, labeled with fluorescent D-amino acids. Black line shows xylose washout. Error bars show 95% confidence intervals. Analysis performed over 680 segmentations from 2 biological replicates. Inset shows micrographs at (i) 5 min and (ii) 65 min following xylose depletion. Micrographs are identically saturated across timepoints. **(B)** Mean EDA-DA AF488 click-labeled puncta per cell (normalized to cell length) for wild-type cells during co-treatments with antibiotics shown. Analysis was performed over 1,533 cells (LB, 5 experimental replicates), 1,063 cells (tunicamycin, 5 experimental replicates), 810 cells (tunicamycin + vancomycin, 3 experimental replicates), 1,081 cells (vancomycin, 4 experimental replicates), 555 cells (fosfomycin control, 4 experimental replicates), and 473 cells (unstained, 4 experimental replicates). All differences between conditions were significant (one-way ANOVA followed by Tukey's HSD post-hoc test, $P<0.01$) with the exception of comparisons between vancomycin, tunicamycin+vancomycin and fosfomycin. Inset: fluorescent micrographs of AF488 labeling in cells cultured with (i) LB alone and (ii) tunicamycin. Micrographs are identically saturated across conditions. Scale bars 5μm.

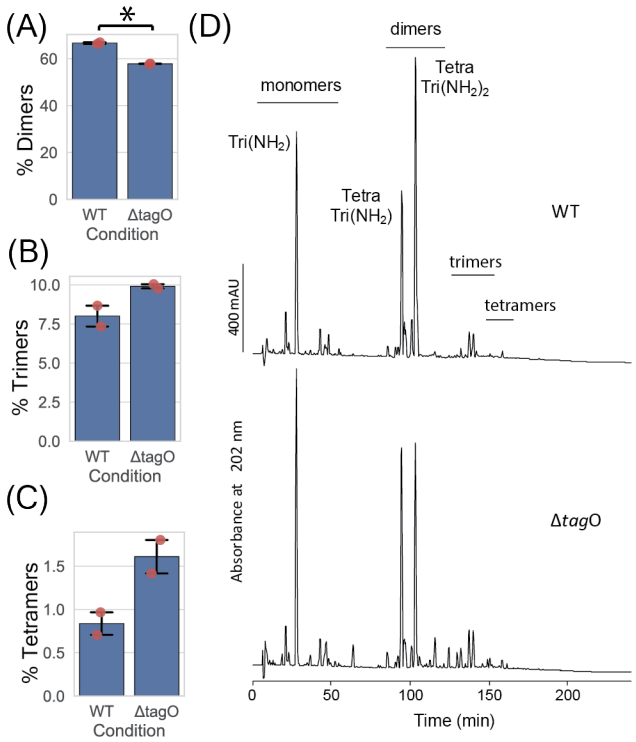

Figure S5: (A-C) Percentage peptidoglycan subunits in **(A)** dimers, **(B)** trimers and **(C)** tetramers. Two biological replicates per strain. Mean values calculated across biological replicates. Error bars show 95% confidence intervals. Individual datapoints shown in red. Statistical significance calculated using Student's T-test, P<0.05. Differences for (B) and (C) are not statistically significant by this metric but reflect visible shifts in high time peaks that are consistent between samples (see (D)). **(D)** High-performance liquid chromatograms of reduced muropeptide samples isolated from wild-type and Δ*tagO* cells. Elution regions of the uncross-linked monomers and cross-linked dimers, trimers and tetramers are shown, and the three main muropeptides are labelled. Tri(NH_2), GlcNAc-MurNAc(red)-L-Ala-D-iGlu-mDap (1 amidation); TetraTri(NH2), GlcNAc-MurNAc(red)-L-Ala-D-iGlu-mDap-D-Ala-mDap-D-iGlu-L-Ala-(GlcNAc)MurNAc(red) (1 amidation); TetraTri(NH2)2, GlcNAc-MurNAc(red)-L-Ala-D-iGlu-mDap-D-Ala-mDap-D-iGlu-L-Ala-(GlcNAc)MurNAc(red) (2 amidations). GlcNAc, N-acetylglucosamine; MurNAc(red), N-acetylmuramitol; L-Ala, L-alanine; D-iGlu, D-isoglutamic acid; mDap, meso-diaminopimelic acid; D-Ala, D-alanine.

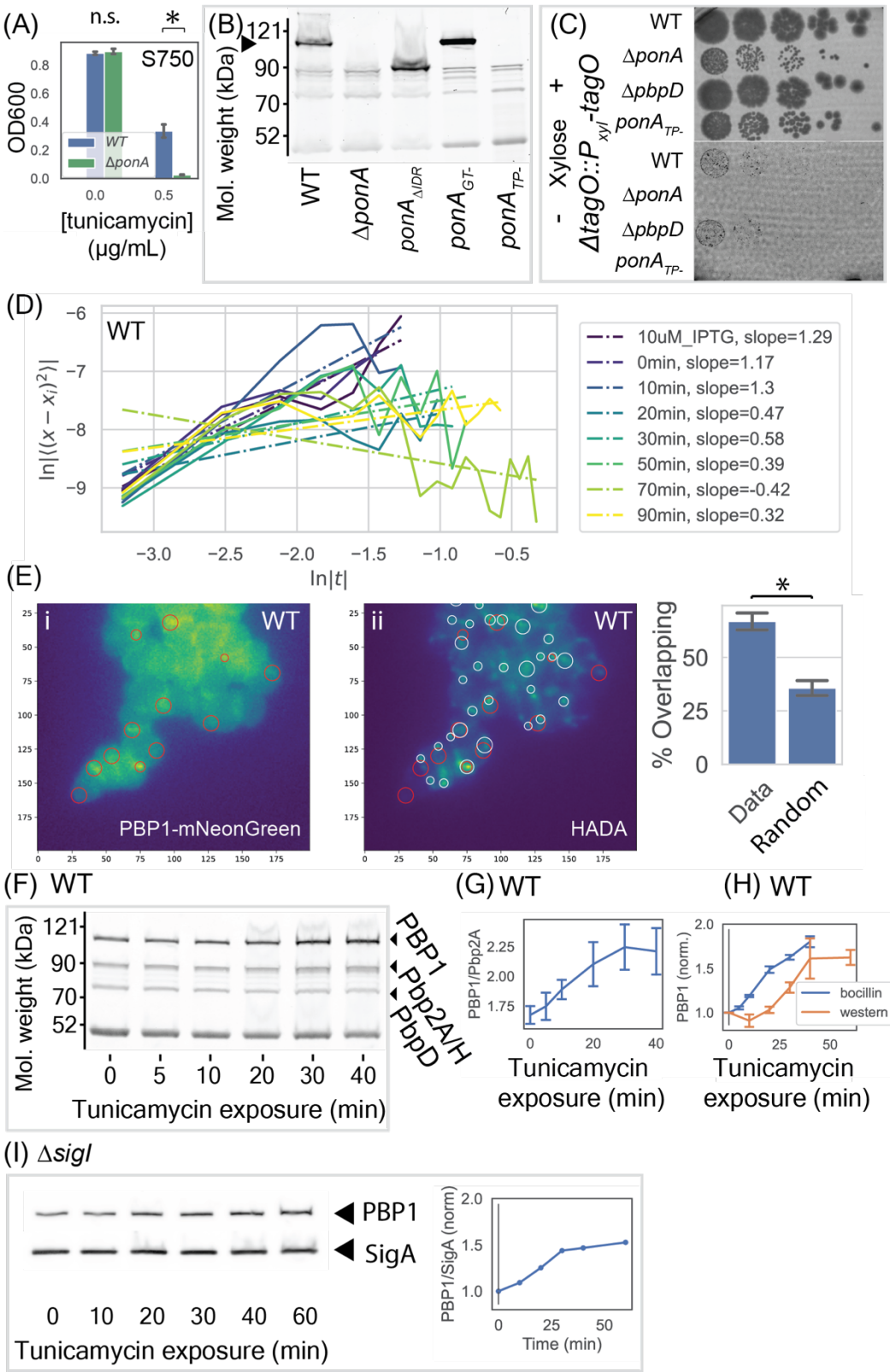

Figure S6: (A) Maximum OD for wild-type and Δ*ponA* cells with and without a low dose of tunicamycin, grown in bulk culture in S750 minimal media. Data shown from one representative biological

replicate out of three, with four technical replicates per biological replicate. Error bars show 95% confidence intervals based on bootstrap analysis. Statistical significance calculated using Student's T-test, P<0.01. **(B)** SDS-PAGE on cell lysates from cultures incubated with fluorescently conjugated bocillin. Black arrow shows wild-type PBP1, which is present in wild-type and $ponA_{GT-}$ strains, shifted in $ponA_{\Delta IDR}$ cells, absent in Δ*ponA* cells, and not labeled in $ponA_{TP-}$ cell lysates. **(C)** Spot assays for WT, Δ*ponA*, $ponA_{TP-}$ and Δ*pbpD* mutant strains in a P_{xylA}-*tagO* background, grown in the presence and absence of 30mM xylose. **(D)** log-log plot of mean-squared displacement vs. time for single molecule tracking of PBP1 puncta, throughout a time course of tunicamycin treatment. Slopes correspond to the diffusion exponent α in Fig. 2D of the main text. Data plotted from one representative biological replicate of three. **(E)** Co-localization of fluorescent puncta within epifluorescent imaging of (i) PBP1-mNeonGreen expressed at a low level alongside the native copy of *ponA*, and (ii) fluorescent labeling with HADA. Cells were imaged following 90 minutes exposure to tunicamycin and a 5-minute incubation with HADA. White circles show computationally detected HADA puncta, red circles show the same for PBP1. Inset: the percentage of PBP1 puncta that overlap with HADA puncta, both for our measured data and for the same PBP1 puncta when distributed randomly throughout the cell masks. Analysis performed on 3,320 PBP1 puncta and 6,253 HADA puncta across two biological replicates. Error bars show 95% confidence intervals based on bootstrap analysis, statistical significance calculated by Student's T-test, P<0.01. **(F)** SDS-PAGE of *B. subtilis* whole cell lysates shows bocillin-PBP binding during tunicamycin treatment. Arrows show PBP1, PBP2A/PBP2B and PbpD bands. Cells were treated with fluorescent bocillin for two minutes prior to cell lysis. One representative sample shown from 3 biological replicates. **(G-H)** Quantification of (F), showing the ratio of **(G)** PBP1 to PBP2A/PBP2B and **(H)** PBP1 to PbpD intensities (normalized to value at 0 min; PbpD staining showed no sustained trend during tunicamycin treatment). Error bars show standard error of the mean across 3 biological replicates. Western blot data reproduced from Fig. 2E. **(I)** Western blot analysis of PBP1 levels during 0.5μg/mL tunicamycin treatment of a Δ*sigI* mutant. Left: Western blot bands for PBP1-FLAG and identically loaded SigA control. Loading volumes normalized based on OD600 readings. Right: Quantification of PBP1 staining, normalized by SigA stain and measured relative to values at 0min tunicamycin treatment. One biological replicate.

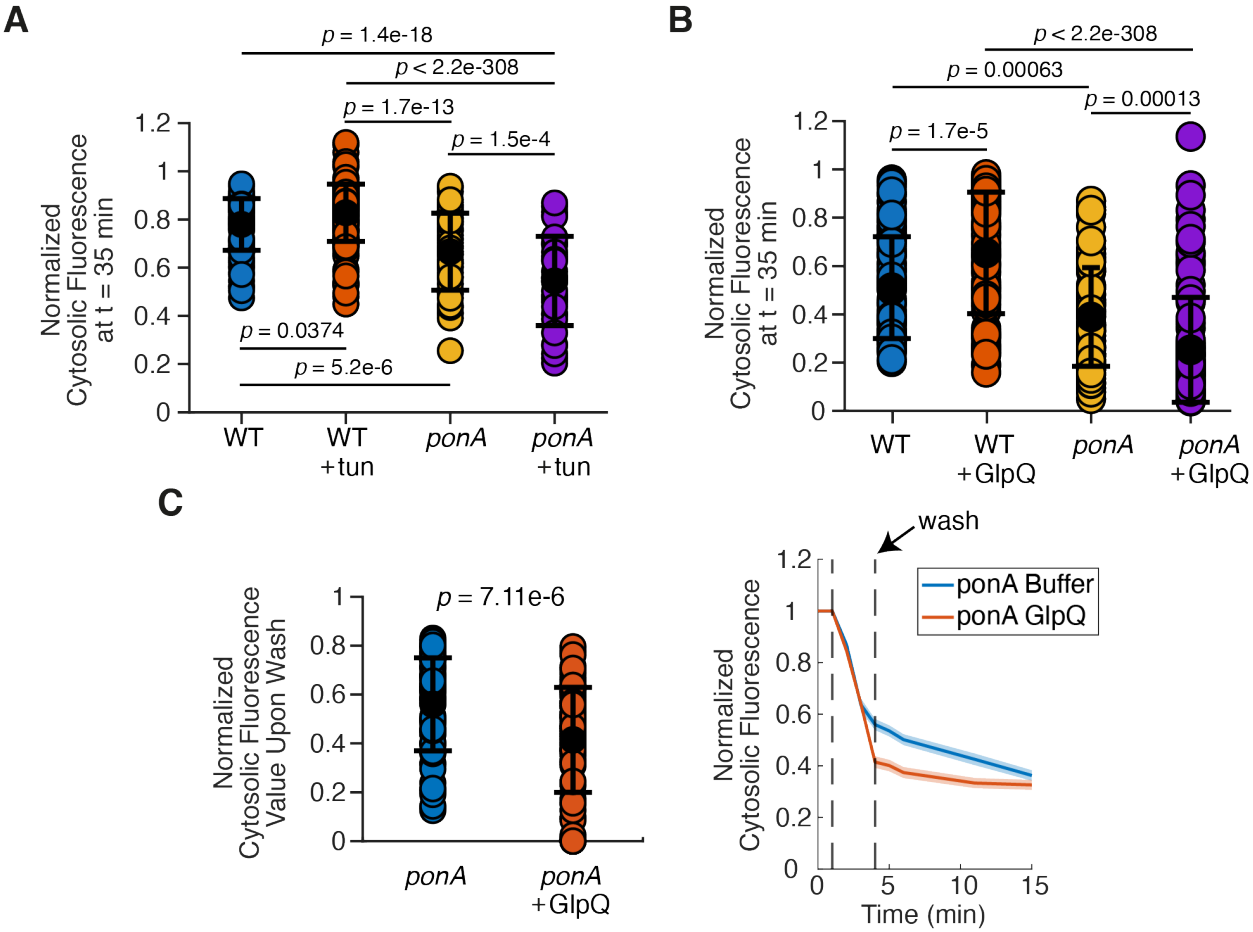

Figure S7: Statistical significance and decay statistics for cell wall permeability assay. (A) mNeonGreen fluorescence at t=35 min for wild-type and Δ*ponA* cells either treated with tunicamycin or untreated. Statistical significance determined via one-way ANOVA (p = 1.9e-27) followed by Tukey's HSD post-hoc test for multiple comparisons (p-values shown in figure). (B) mNeonGreen fluorescence at t=35 min for wild-type and Δ*ponA* cells either treated with GlpQ in PBS or PBS alone. Statistical significance determined via one-way ANOVA (p = 8.7e-32) followed by Tukey's HSD post-hoc test for multiple comparisons. All p-values are shown in the figure, except for wild-type untreated vs. *ponA* + GlpQ (p = 2.5e-18) and WT + GlpQ vs *ponA* untreated (p = 9.9e-15). (C) mUbiquitin fluorescence upon wash (as indicated by the arrow on the fluorescence vs time graph, right) following incubation of Δ*ponA* cells with detergent +/- GlpQ. Statistical significance calculated using Student's T-test with p = 7.11e-6.

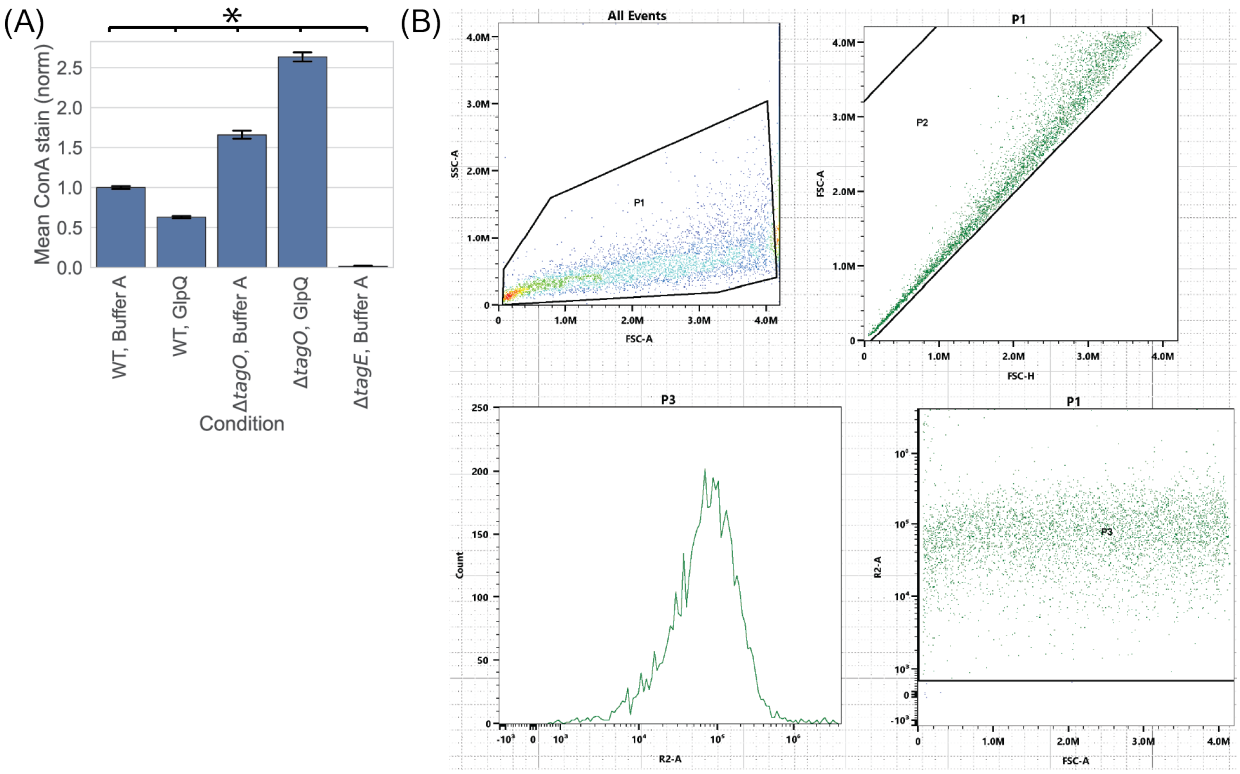

Figure S8: (A) Mean fluorescence intensity of Concanavalin A-AlexaFluor647 cell staining, following incubation either with PBS + Buffer A, or with PBS + GlpQ, measured by flow cytometry. GlpQ-treated cells show decreased Concanavalin A staining relative to PBS-treated cells, consistent with GlpQ enzymatically cleaving teichoic acids from the cell wall. Δ*tagO* cells show no such decrease in Concanavalin A staining upon GlpQ incubation, and Δ*tagE* cells lacking the enzyme responsible for teichoic acid glycosylation show negligible labeling. We observed increased Concanavalin A-staining in Δ*tagO* cells relative to wild-type that was amplified during GlpQ treatment, possibly due to the clumping phenotype of this mutant. Error bars show 95% confidence intervals across 3 biological replicates, 10,000 samples per replicate. All conditions show statistically significant differences as measured by one-way ANOVA followed by Tukey's HSD post-hoc test, $P<0.01$. **(B)** Representative example of flow cytometry gating process used to generate data in (A).

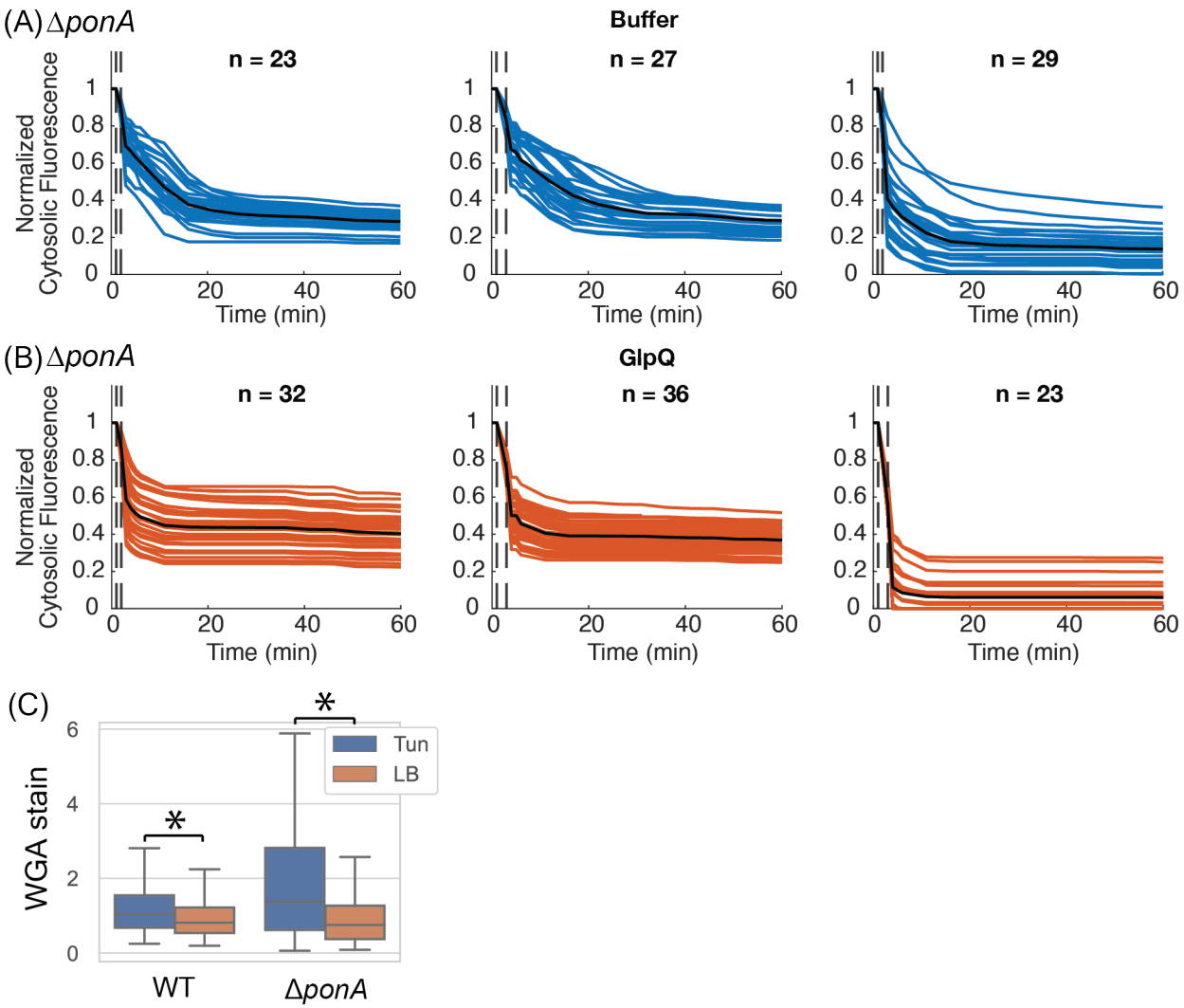

524

525 **Figure S9:** Ubiquitin-FlAsH immediately leaves the cytosol upon wall teichoic acid digestion and
526 simultaneous lysis in Δ*ponA* cells. **(A-B)** Individual Ubiquitin-FlAsH fluorescent traces and experimental
527 replicates following 2 min incubation with PBS +5% N-lauroylsarcosine and either **(A)** Buffer A alone, or
528 **(B)** 40uM GlpQ. Cell counts are shown in figure captions. **(C)** Fluorescence of cells labeled with a wheat-
529 germ agglutinin-AlexaFluor488 conjugate after incubation with LB alone or LB supplemented with
530 tunicamycin for either 10 min (wild-type) or 20 min (Δ*ponA*). Wild-type LB: 538 cells. Wild-type
531 tunicamycin: 271 cells. Δ*ponA* LB: 285 cells. Δ*ponA* tunicamycin: 288 cells. 3 biological replicates per
532 condition. Significance tested by Student's T-test, P<0.01.

533

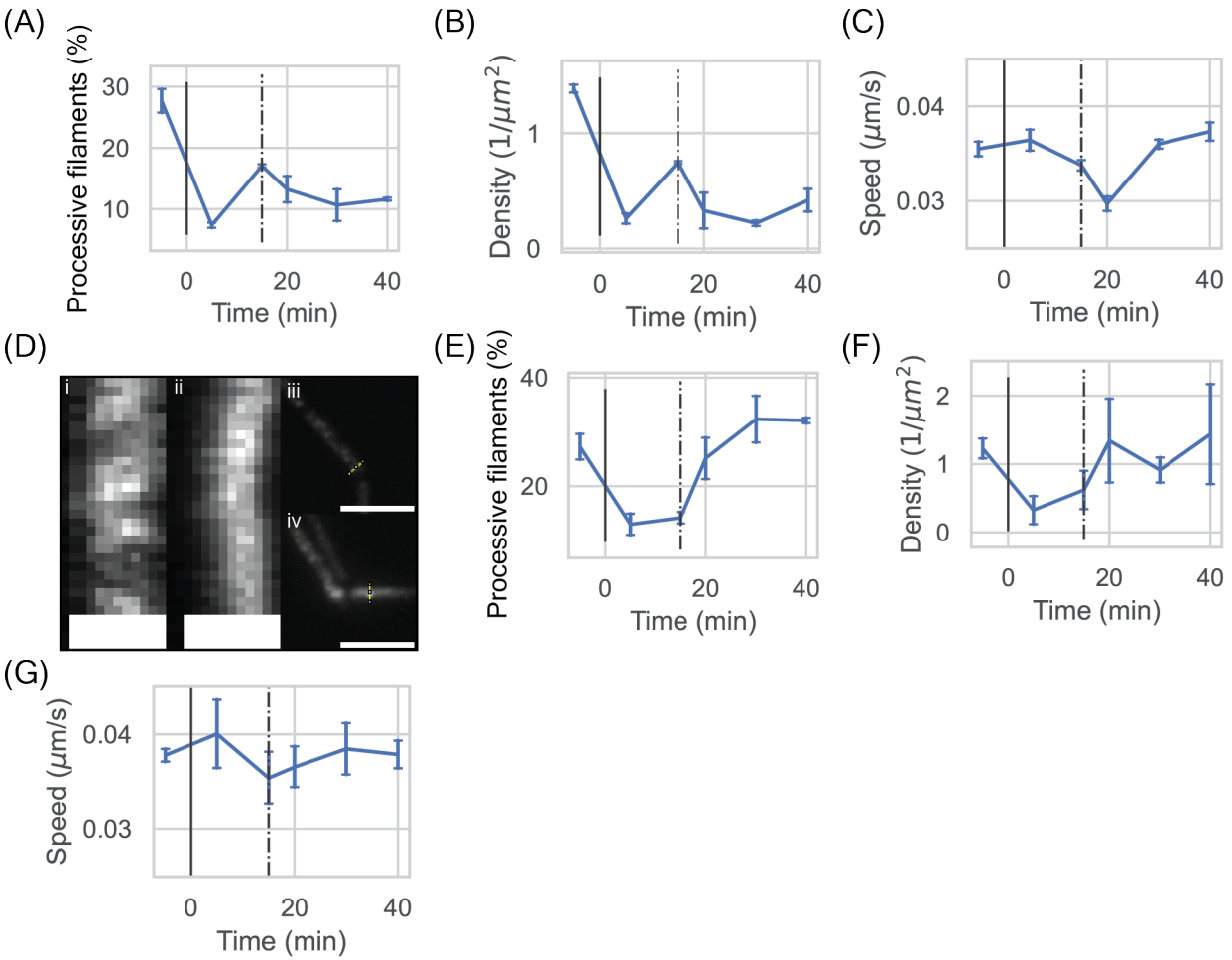

Figure S10: (A-C) Mbl-sfGFP activity time course during 25µM GlpQ treatment. Analysis performed on 10,976 discrete filament tracks from 2 biological replicates. **(A)** Percentage of processive filaments. **(B)** Spatial density of processive Mbl-sfGFP filaments. **(C)** Speed of processive Mbl-sfGFP filaments. All error bars show 95% confidence intervals across biological replicates based on bootstrap analysis. **(D)** Representative kymographs from TIRF imaging of (i) growing and (ii) non-growing wild-type cells 35 min after release from GlpQ treatment. Scale bars 1µm. (iii-iv) TIRF micrographs showing whole cells during a single timepoint of kymographs in (i-ii) respectively. Yellow lines show kymograph traces. Scale bars 5µm. **(E-G)** Mbl-sfGFP and MreB-mNeonGreen activity time course during PBS treatment. Analysis performed on 11,150 discrete filament tracks from 3 independent experiments. Data pooled from experiments with 15min and 20min PBS exposure. **(E)** Percentage of processive filaments. **(F)** Spatial density of processive Mbl-sfGFP filaments. **(G)** Speed of processive filaments.

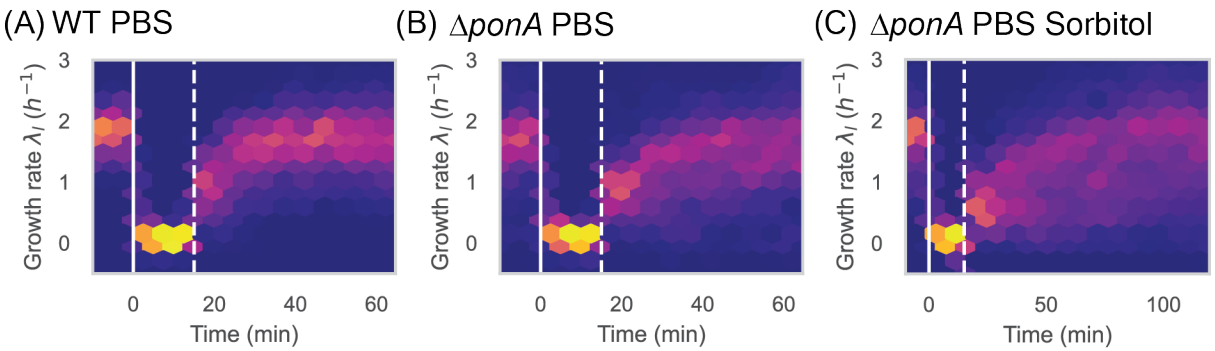

Figure S11: (A-B) Heat maps showing growth rate $\lambda_l = \frac{1}{l}\frac{dl}{dt}$ during recovery after incubation with either PBS + denatured GlpQ or GlpQ buffer for 15 min. **(A)** wild-type cells (3,830 discrete tracks, two independent experiments with denatured GlpQ, one with equivalent volume GlpQ buffer, no differences between conditions observed). **(B)** Δ*ponA* cells (2,142 discrete cell tracks, 3 biological replicates). **(C)** Heatmap showing Δ*ponA* cell length growth rate $\lambda_l = \frac{1}{l}\frac{dl}{dt}$ following 15-minute incubation with PBS + GlpQ Buffer (*not* GlpQ enzyme) (7,097 discrete cell tracks, 3 biological replicates), where exit from incubation is coupled to a 500mM Sorbitol hyperosmotic shock. Solid line shows onset of PBS incubation, dotted line shows exit into LB + Sorbitol.

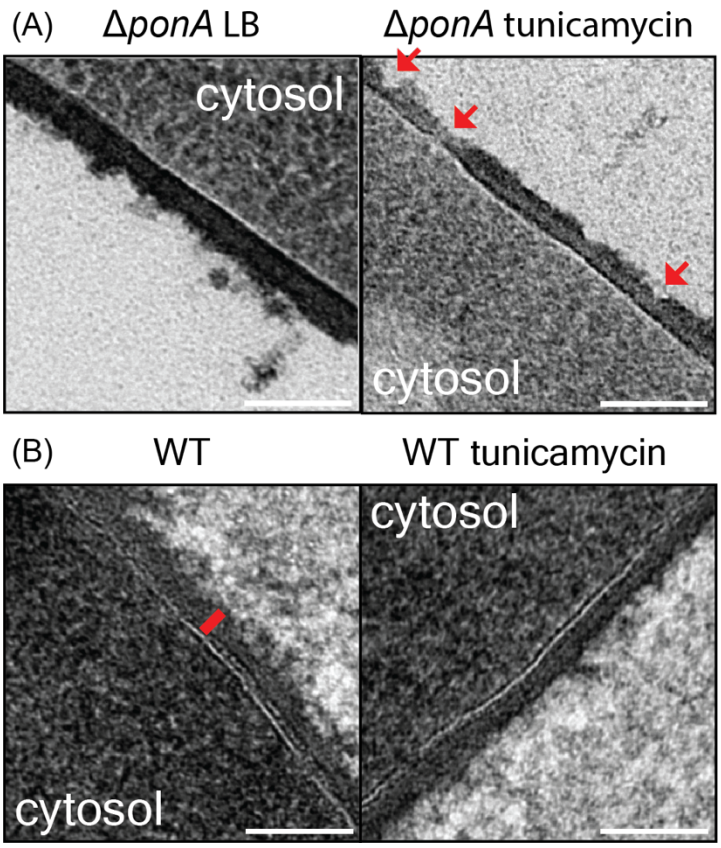

Figure S12: Transmission electron micrographs of the sidewall of exponentially growing cells grown in either LB or LB supplemented with 0.5μg/mL tunicamycin for 30 min. Scale bars 100nm. **(A)** Δ*ponA* cells. Red arrows show sites of severe cell wall thinning during tunicamycin treatment. **(B)** Wild-type cells. Red bar shows the region used to calculate cell wall thickness, measured from the edge of the cell membrane (white line).

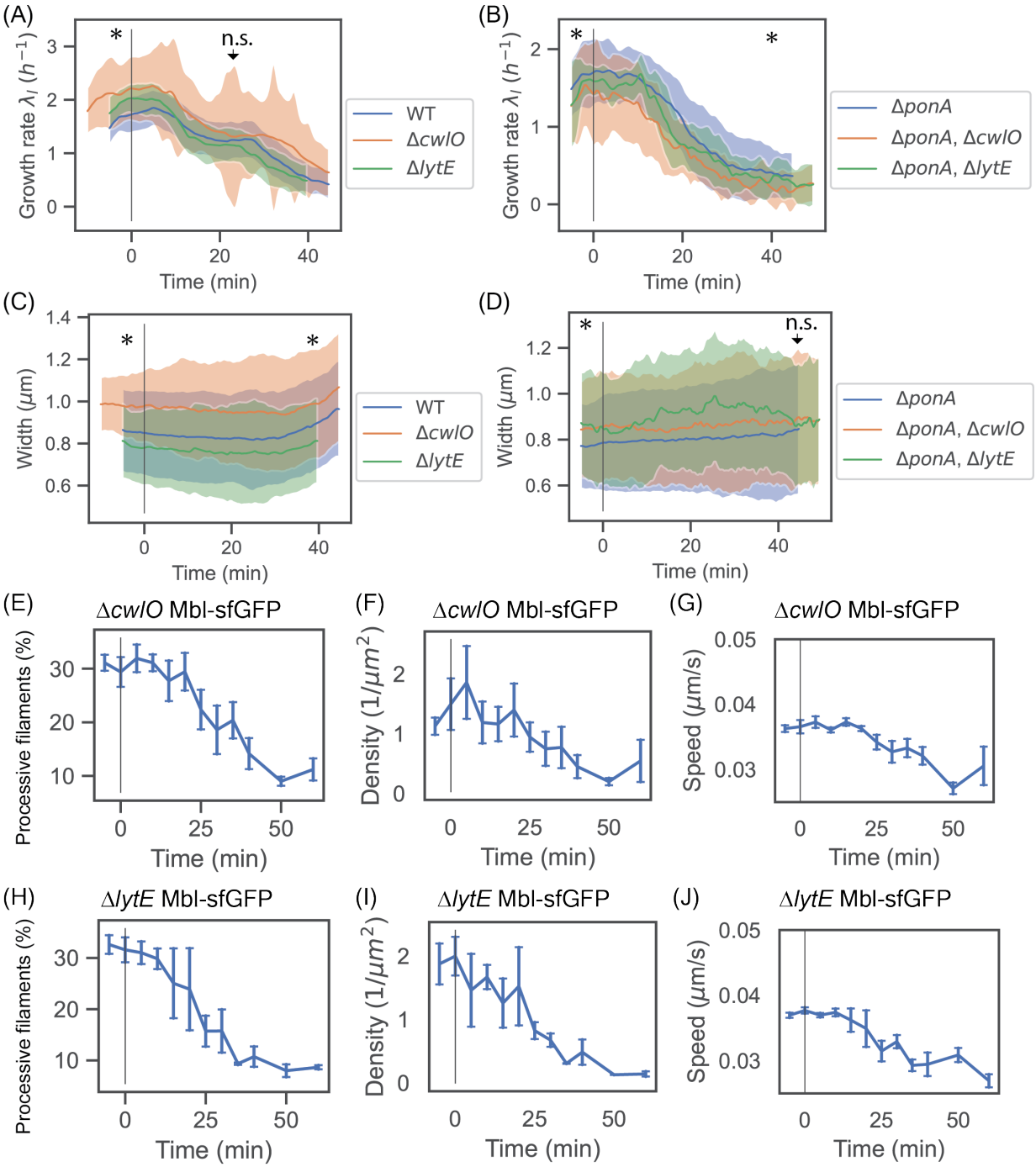

Figure S13. (A-B) Cell elongation rate during tunicamycin treatment for **(A)** wild-type, Δ*cwlO* and Δ*lytE* cells and **(B)** Δ*ponA*, Δ*ponA* Δ*cwlO* and Δ*ponA* Δ*lytE* cells. **(A)** Strains showed statistically significant differences in initial growth rate (time=-5min), but converged to a plateau growth rate that did not reject the null (equal) hypothesis (t=22 min following tunicamycin treatment). Significance calculated using Student's T-test, P<0.01. Analysis performed over 1,091 discrete cell tracks from 5 experimental

568 replicates (Δ*cwlO*), and 1,277 discrete cell tracks plotted from three experimental replicates (Δ*lytE*). Wild-
569 type data replotted from Fig. 1B. **(B)** Hydrolase mutants showed significantly lower initial growth rates
570 than the Δ*ponA* mutant (first measured timepoint), while the Δ*ponA* Δ*cwlO* mutant showed a significantly
571 lower final growth rate than the Δ*ponA* mutant. All strains lacked the plateau in growth rate of wild-type
572 cells. Analysis performed over 164 discrete cell tracks from two experimental replicates (Δ*ponA* Δ*cwlO*),
573 and 105 discrete cell tracks plotted from two experimental replicates (Δ*ponA* Δ*lytE*). Δ*ponA* data replotted
574 from Fig. 2A. **(C-D)** Cell width dynamics during tunicamycin treatment for **(C)** wild-type, Δ*cwlO* and Δ*lytE*
575 cells and **(D)** Δ*ponA*, Δ*ponA* Δ*cwlO* and Δ*ponA* Δ*lytE* cells. **(C)** Strains showed statistically significant
576 differences in width throughout, calculated using Student's T-test, P<0.01 at the first and last measured
577 timepoints. All strains display characteristic cell widening at long times. Analysis performed over 1,746
578 discrete cell tracks from 5 experimental replicates (Δ*cwlO*), and 2,432 discrete cell tracks from three
579 experimental replicates (Δ*lytE*). Wild-type data replotted from Fig. 1B. **(D)** Hydrolase mutants showed
580 statistically significant differences in width from Δ*ponA* mutant at the first measured timepoint, but
581 showed no significant differences at the final timepoint (t=45 min tunicamycin exposure) and consistently
582 lacked the characteristic cell widening of wild-type cells at long times. Significance calculated using
583 Student's T-test, P<0.01. Analysis performed over 1,747 discrete cell tracks from five biological replicates
584 (Δ*ponA*), 632 discrete cell tracks from two experimental replicates (Δ*ponA* Δ*cwlO*), and 585 discrete cell
585 tracks from two experimental replicates (Δ*ponA* Δ*lytE*). **(E-J)** Rod complex dynamics measured by tracking
586 Mbl-sfGFP filaments during tunicamycin treatment for **(E-G)** Δ*cwlO* and **(H-J)** Δ*lytE* cells. **(E, H)** Percentage
587 of processive filaments. **(F, I)** Spatial density of processive filaments. **(G, J)** Average speed of processive
588 filaments. Analysis performed over 37,707 tracked filaments from four biological replicates (Δ*cwlO*) and
589 45,748 tracked filaments from three biological replicates (Δ*lytE*).

590

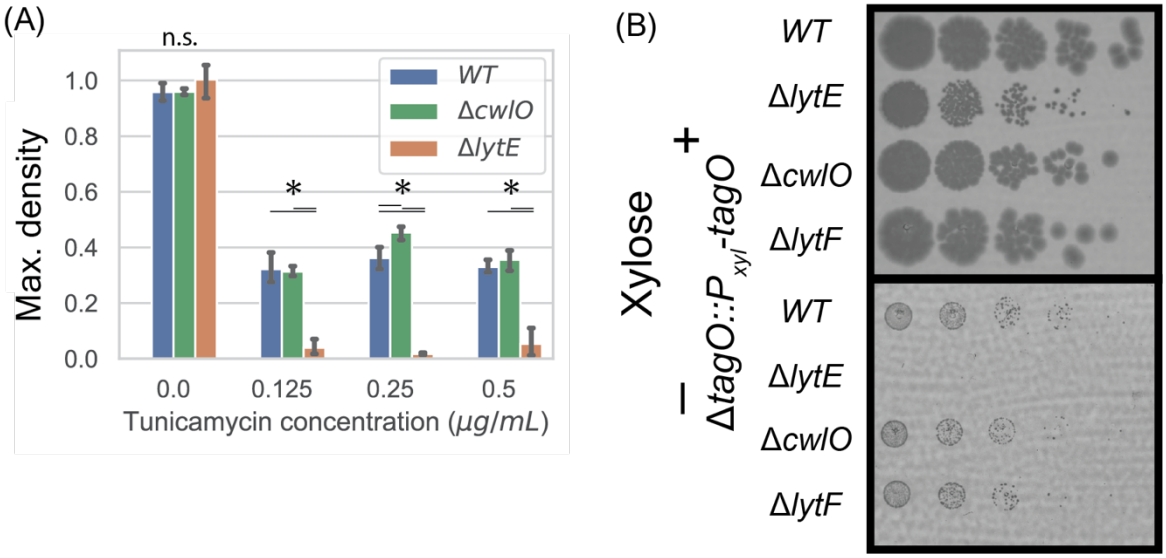

Figure S14. (A) Saturating culture density during growth in various concentrations of tunicamycin for wild-type, Δ*cwlO* and Δ*lytE* cells. Data shown from one representative biological replicate out of two, with four technical replicates per biological replicate. Error bars show 95% confidence intervals based on bootstrap analysis. Statistical significance tested with one-way ANOVA followed by Tukey's HSD post-hoc test for different concentrations of tunicamycin, P<0.01. **(B)** Spot assays showing growth with and without *tagO* transcriptional inhibition in P_{xylA}-*tagO* cells with the mutant backgrounds shown (two biological replicates).

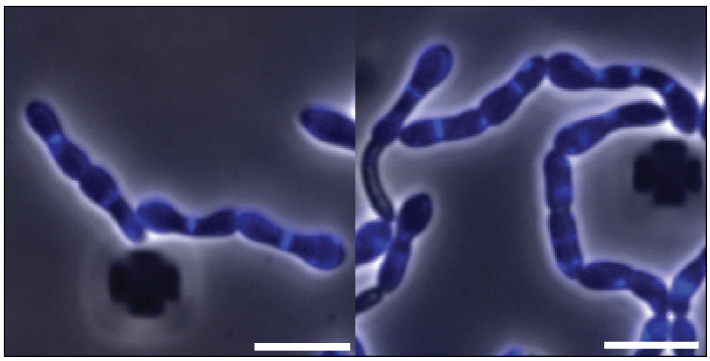

Figure S15: Cell bulging occurs gradually a "dumbbell" phenotype during teichoic acid depletion. Cell wall bulges become more prevalent with increasing distance from internal septa, presumably due to septal reinforcement of the local cell wall. Micrographs show HADA fluorescent staining in blue, superimposed over phase contrast images of cells following 45 min exposure to 0.5μg/mL tunicamycin and 5min HADA incubation. Scale bars 5μm. One biological replicate.

606 **Video S1:** 100X Phase timelapse of wild-type growth during 0.5 μg/mL tunicamycin treatment.
607 tunicamycin exposure starts at 5min. Time step=20s. Scale bar 5μm.

608 **Video S2:** 100X TIRF imaging of Mbl-sfGFP motion in wild-type cells grown in LB. Time step=2s. Scale bar
609 5μm.

610 **Video S3:** 100X TIRF imaging of Mbl-sfGFP motion in wild-type cells grown in LB. Time step=2s. Scale bar
611 5μm.

612 **Video S4:** 100X TIRF imaging of Mbl-sfGFP motion in wild-type cells grown in LB, then treated with 0.5
613 μg/mL tunicamycin for 30min. Time step=2s. Scale bar 5μm.

614 **Video S5:** 100X TIRF imaging of Mbl-sfGFP motion in wild-type cells grown in LB, then treated with 0.5
615 μg/mL tunicamycin for 30min. Time step=2s. Scale bar 5μm.

616 **Video S6:** 100X TIRF imaging of Mbl-sfGFP motion in wild-type cells grown in LB, then treated with 0.5
617 μg/mL tunicamycin for 60min. Time step=2s. Scale bar 5μm.

618 **Video S7:** 100X TIRF imaging of Mbl-sfGFP motion in wild-type cells grown in LB, then treated with 0.5
619 μg/mL tunicamycin for 60min. Time step=2s. Scale bar 5μm.

620 **Video S8:** 100X TIRF imaging of PBP1-mNeonGreen dynamics during steady state growth, driven from a
621 heterologous HyperSpank promoter with 10μM IPTG in addition to the endogenous copy of *ponA*. Time
622 step = 500ms. Scale bar 5μm.

623 **Video S9:** 100X TIRF imaging of PBP1-mNeonGreen dynamics, driven from a heterologous HyperSpank
624 promoter with 10μM IPTG in addition to the endogenous copy of *ponA*. Cells treated with 0.5 μg/mL
625 tunicamycin for 90min. Time step = 500ms. Scale bar 5μm.

626 **Video S10:** 100X TIRF imaging of Mbl-sfGFP motion in Δ*ponA* cells grown in LB supplemented with
627 10mM $MgCl_2$. Time step=2s. Scale bar 5μm.

628 **Video S11:** 100X TIRF imaging of Mbl-sfGFP motion in Δ*ponA* cells grown in LB supplemented with
629 10mM $MgCl_2$, then treated with 0.5 μg/mL tunicamycin for 30min. Time step=2s. Scale bar 5μm.

630 **Video S12:** 100X TIRF imaging of Mbl-sfGFP motion in growing wild-type cells treated with 25uM GlpQ
631 for 15 minutes. Timelapse taken 25 min post release into LB. Time step=2s. Scale bar 5μm.

632 **Video S13:** 100X TIRF imaging of Mbl-sfGFP motion in growing wild-type cells treated with 25uM GlpQ
633 for 15 minutes. Timelapse taken 35 min post release into LB. Time step=2s. Scale bar 5μm.

634 **Video S14:** 100X TIRF imaging of Mbl-sfGFP in non-growing wild-type cells treated with 25uM GlpQ for
635 15 minutes. Timelapse taken 25 min post release into LB. Time step=2s. Scale bar 5μm.

636 **Video S15:** 100X TIRF imaging of Mbl-sfGFP in non-growing wild-type cells treated with 25uM GlpQ for
637 15 minutes. Timelapse taken 35 min post release into LB. Time step=2s. Scale bar 5μm.